

Robust optical features of fine mode size distributions: Application to the Québec smoke event of 2002

N. T. O'Neill¹ and S. Thulasiraman

CARTEL, Université de Sherbrooke, Sherbrooke, Québec, Canada

T. F. Eck²

NASA Goddard Space Flight Center, Greenbelt, Maryland, USA

J. S. Reid

Naval Research Laboratory, Monterey, California, USA

Received 23 June 2004; revised 3 March 2005; accepted 21 March 2005; published 8 June 2005.

[1] Simple relationships involving the fundamental parameters of fine mode aerosol optical depth (τ_f), Angstrom exponent (α_f) and its derivative (α'_f) as near-monotonic functions of the effective van de Hulst parameter ($\rho_{\text{eff},f} = 2 (2 \pi r_{\text{eff},f}/\lambda) |m - 1|$) were derived for the conceptual case of a log-translatable particle size distribution (LTPSD). This notion is useful in the interpretation of real sunphotometer data; the fine mode size distribution often approximates a LTPSD while departures from this behavior become more readily understood once one understands the first order optics. The near dependency of the fine mode optical parameters on $\rho_{\text{eff},f}$ was also exploited to obtain an explicit expression for $\rho_{\text{eff},f}$ as a function of α_f and α'_f . The relationships were applied to a representative case study to demonstrate their general applicability and then to the specific case of the July 2002 Québec smoke event. A number of illustrations were given where the coherency of the derived relations indicated that the LTPSD concept was often a good approximation to reality. The analysis of the Québec-smoke extinction data showed the existence of a weak but systematic dependence of the Angstrom exponents on smoke trajectory time and by inference a steady growth in particle size with time. The variation of $r_{\text{eff},f}$ (derived from AERONET inversions) was however observed to be inconsistent with this dependence unless one redefined this parameter in terms of the clearly delineated peak of the asymmetric fine mode particle size distribution (PSD). This definition led to a re-computed temporal rate of increase in $r_{\text{eff},f}$ which was coherent with the variation of the Angstrom parameters and which was coherent with a simple coagulative model based on conservation of volume. It was demonstrated that trajectory time was essentially a proxy variable for $r_{\text{eff},f}$ and more fundamentally $\rho_{\text{eff},f}$ (as predicted by the LTPSD relations). A similar proxy argument could be applied to the dependence of the Angstrom exponent on optical depth but such arguments are tempered by the relative variations of fine-mode abundance (A_f) and particle size (by the value of the parameter $\gamma = d \log A_f / d \log r_{\text{eff},f}$).

Citation: O'Neill, N. T., S. Thulasiraman, T. F. Eck, and J. S. Reid (2005), Robust optical features of fine mode size distributions: Application to the Québec smoke event of 2002, *J. Geophys. Res.*, *110*, D11207, doi:10.1029/2004JD005157.

1. Introduction

[2] Optical data and in particular sunphotometer data are important sources of information on the behavior of aerosol particles. While considerable effort has gone into retrieval

algorithms combining sunphotometer and sky radiometry data there is an ever present danger that such techniques, especially in an operational setting, tend to obscure the relatively simple physics which generally characterize the greater portion of the optical variance. This has spawned a natural movement to better understand the optical influences which generate the more robust features of inverted information.

[3] A certain amount of research effort in recent years has focussed on robust and easily comparable measures of particle number and particle size such as the aerosol optical depth (AOD or τ_a), Angstrom exponents (α), and effective

¹Formerly at NASA Goddard Space Flight Center, Greenbelt, Maryland, USA.

²Also at Goddard Earth Sciences and Technology Center, University of Maryland-Baltimore County, Baltimore, Maryland, USA.

particle size (r_{eff}). To a certain extent there is a lack of universality in the literature inasmuch as no explicit theoretical framework exists to explain the inter-relationship of first order features in optical space as well as the links between robust parameters in optical space and microphysical space.

[4] The fine mode of the typically bi-modal aerosol particle size distribution (PSD) lends itself to an analysis in terms of robust first-order parameters because it essentially behaves in a conceptually simple manner; it varies little in terms of PSD width while typically exhibiting large variations in PSD amplitude and bulk size indicators such as the modal radius or $r_{\text{eff},f}$. This simplistic behavior leads to analytical formulations which are surprisingly general in application.

[5] Smoke represents a class of fine mode aerosol particles whose first order optical parameters have been studied in some detail (see, for example, *Holben et al.* [1996], *Remer et al.* [1998], and *Reid et al.* [1998, 1999] for their work in the context of Amazonian smoke, *Eck et al.* [2001] on the ZIBBEE experiment in southern Africa, and *O'Neill et al.* [2002, and references therein] for research focused on Boreal-forest smoke properties). Smoke events provide rather unique experiments for the study of fine mode optics since the presence of smoke is easily recognized in ground-based and satellite data, sources are readily pin-pointed and the signal is dominant for periods ranging from hours to days.

[6] In this paper we develop relationships between the key fine mode parameters of optical depth (τ_f), Angstrom exponent (α_f), second order Angstrom exponent (α'_f) and the effective radius ($r_{\text{eff},f}$) based on a simple conceptual model of the fine mode PSD (where the three optical parameters were computed at a reference wavelength of 500 nm from a second order polynomial fit to AOD spectra; see the sunphotometer processing section below). The applicability of these (purely sunphotometric) relationships will be investigated using AERONET inversion products on a representative case study. We then investigate the behavior of the fine mode parameters during the Québec smoke event of July 2002 [*Colarco et al.*, 2004] and attempt to demonstrate certain robust behavior which characterized these aerosol particles. The analysis of the fine mode case study will, at the same time, permit us to illustrate the general applicability of the first-order conceptual relationships.

2. Robust Optical Features of Fine-Mode Particles: Fundamental Relations

2.1. LTPSD (Log-Translatable PSD) Relations

[7] A convenient conceptual model for fine mode PSD variations is to restrict particle number changes to generic variations in bulk abundance (i.e. equally distributed variations in columnar number density across the total size spectrum) and/or to restrict size changes to logarithmic translations (see Appendix A). This is illustrated in Figure A1 where the simulated change from the left hand PSDs to the right hand PSDs involves (a) a simple translation and (b) a particle number increase which does not change the form of the PSD. The result of these simple perturbations is to conserve geometric standard deviations and logarithmically translate geometric means by a fixed amount (independent of the type of distribution). For brevity we will refer to a PSD which has these properties

as a log-translatable PSD or LTPSD. A LTPSD approximates the effects of relative humidity-induced particle growth where $r(\text{RH})/r(0) \approx f(\text{RH})$ for all but the smallest radius particles. It also represents coagulative aging in smoke and to a lesser extent the combination of coagulative aging and diffusion-limited growth (the variation of the PSD standard deviation being anti-correlated with particle size but relatively weak in magnitude [*Reid et al.*, 1999]). While the fine-mode PSDs derived from AERONET inversions of *Dubovik and King* [2000] will, in general, depart to some degree from this simple conceptual model, the LTPSD concept nonetheless provides a baseline which facilitates the optical analysis of more complex PSDs.

[8] In Appendix B we demonstrate that the LTPSD averaged extinction efficiency ($\langle Q_{\text{ext}} \rangle = \tau_f/S_f$), the fine-mode Angstrom exponent (α_f) and the spectral derivative of the fine-mode Angstrom exponent (α'_f) are monotonic functions of the effective van de Hulst's phase shift parameter [*van de Hulst*, 1957];

$$\rho_{\text{eff},f} = 2 \frac{2\pi r_{\text{eff},f}}{\lambda} |m - 1| = 2 x_{\text{eff},f} |m - 1| \quad (1)$$

where S_f is the fine mode (cross-sectional) surface PSD, m is the complex refractive index and $r_{\text{eff},f}$ is the effective radius of the fine mode PSD [*Hansen and Travis*, 1974]. Equation (1) is intuitive: if the Mie parameters derived for monodisperse distributions are near monotonic functions of $\rho = 2 (2 \pi r/\lambda) |m - 1|$ then it follows that, for PSD averaged parameters, one should hope for some approximate level of monotonicity as a function of $\rho_{\text{eff},f}$. The Mie calculations of Figure 1 demonstrate this near-monotonicity for three smoke-particle simulations chosen to represent three extremes of biomass burning refractive index. Each curve was generated for a log-normal PSD of fixed geometric standard deviation (the classic example of a LTPSD). The curves are universal in that they apply to any combination of $r_{\text{eff},f}$ and λ at a given value of $\rho_{\text{eff},f}$. At the same time they are something less than universal in terms of (the complex part of) the refractive index since the dispersion between the three cases increases from $\langle Q_{\text{ext}} \rangle$ to α_f to α'_f . Likewise, an increase in the width of the PSD (not shown in Figure 1) tends to decrease the amplitude of all curves and flatten out the dependence on $\rho_{\text{eff},f}$. It is our contention however that the general optical behavior of fine mode aerosol particles often resembles the behavior predicted for a LTPSD. This hypothesis leads to some useful optical approximations which explain much of the variation seen in AOD spectra.

[9] Figure 2a demonstrates this near monotonic dependency of τ_f/S_f ($\langle Q_{\text{ext}} \rangle$) on $r_{\text{eff},f}$ and $\rho_{\text{eff},f}$ for a set of representative AOD spectra (see the data processing section for details on the CIMEL sunphotometer computations). These data were acquired at the AERONET Norfolk, Virginia site during the complete month of July of 2002: there was no geo-physical strategy in selecting Norfolk, all other sites tested show similar behavior. The fine mode parameters of this figure, including $r_{\text{eff},f}$ and $\rho_{\text{eff},f}$ were extracted or computed from the AERONET inversion results [*Dubovik and King*, 2000]. The mean and standard deviation of the geometric standard deviation ($\sigma_{V,f}$) of the fine mode volume PSDs for these points was 1.5 and 0.1. In

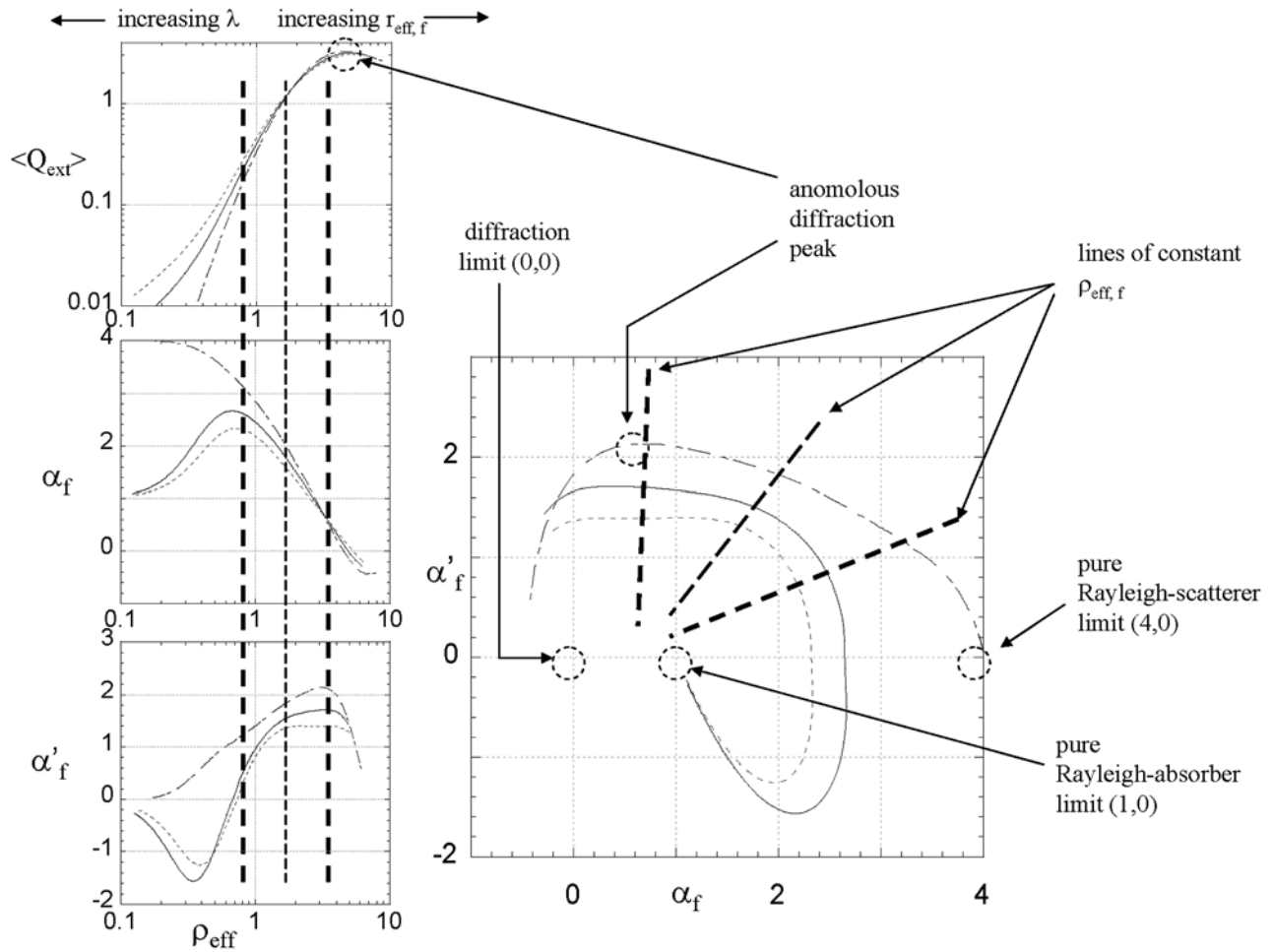


Figure 1. $\langle Q_{\text{ext}} \rangle$, α_f and α'_f curves for a log-normal distribution of variable geometric mean radius, variable wavelength and a fixed geometric standard deviation of σ_f ($= \sigma_v = \sigma_s = \sigma_\lambda$ for a log-normal distribution) = 1.5. Three cases are plotted: (1) dash-dot curve; nonabsorbing homogeneous sphere of refractive index $m = 1.5 - 0i$. (2) Solid curve; soot core of refractive index $1.8 - 0.6i$ surrounded by a nonabsorbing shell of refractive index $= 1.5 - 0i$ (6% by mass as per Reid *et al.* [1999] with a volume-weighted average refractive index of $1.514 - 0.029i$). (3) Dotted curve; as for case 2 with a core mass fraction of 12% and an average refractive index of $1.529 - 0.058i$. The bold dashed lines roughly indicate the limits of fine mode $\rho_{\text{eff},f}$ for sunphotometric wavelengths between 380 and 1020 nm. At 500 nm the range of $\rho_{\text{eff},f} = 0.1$ to 10 approximately represents an $r_{\text{eff},f}$ range of 0.008 to 0.8 μm .

the first column of graphs one can note the dramatic increase in correlation with $r_{\text{eff},f}$ effected by the S_f normalization of τ_f (at 500 nm). In the second column we have displayed 380 and 870 nm as well as the 500 nm data as a function of $x_{\text{eff},f} = 2 \pi r_{\text{eff},f} / \lambda$ (effective size parameter) in order to demonstrate the trend towards a single monotonic function of $\rho_{\text{eff},f}$. The almost equally dramatic increase in correlation in going from τ_f/S_f vs $x_{\text{eff},f}$ to τ_f/S_f vs $\rho_{\text{eff},f}$ (last row of the second column of graphs to the last row of the third column of graphs) helps to demonstrate the validity of the LTPSD concept and also shows that refractive index is a necessary component in reducing the point scatter. We caution however that this last observation is a reflection of the variability in the nominal value of the refractive index extracted from the inversion process and may not be indicative of improvements in correlation brought about by the elimination of effects induced by real variations in the refractive index.

[10] In Appendix B we show that the assumption of a near monotonic dependency on $\rho_{\text{eff},f}$ leads to simple and elegant dependencies between the fundamental spectral curvature parameters, viz;

$$\alpha_f = \frac{d \log(\tau_f/S_f)}{d \log \rho_{\text{eff},f}} \quad (2)$$

$$\alpha'_f = - \frac{d \alpha_f}{d \ln \rho_{\text{eff},f}} \quad (3)$$

[11] In this paper we use “log” to represent “log₁₀” (the more popular logarithm for expressing measured optical parameters) and “ln” to represent the natural log when we want to avoid encumbering the equations with inter-log transformation constants. According to equation (2), the

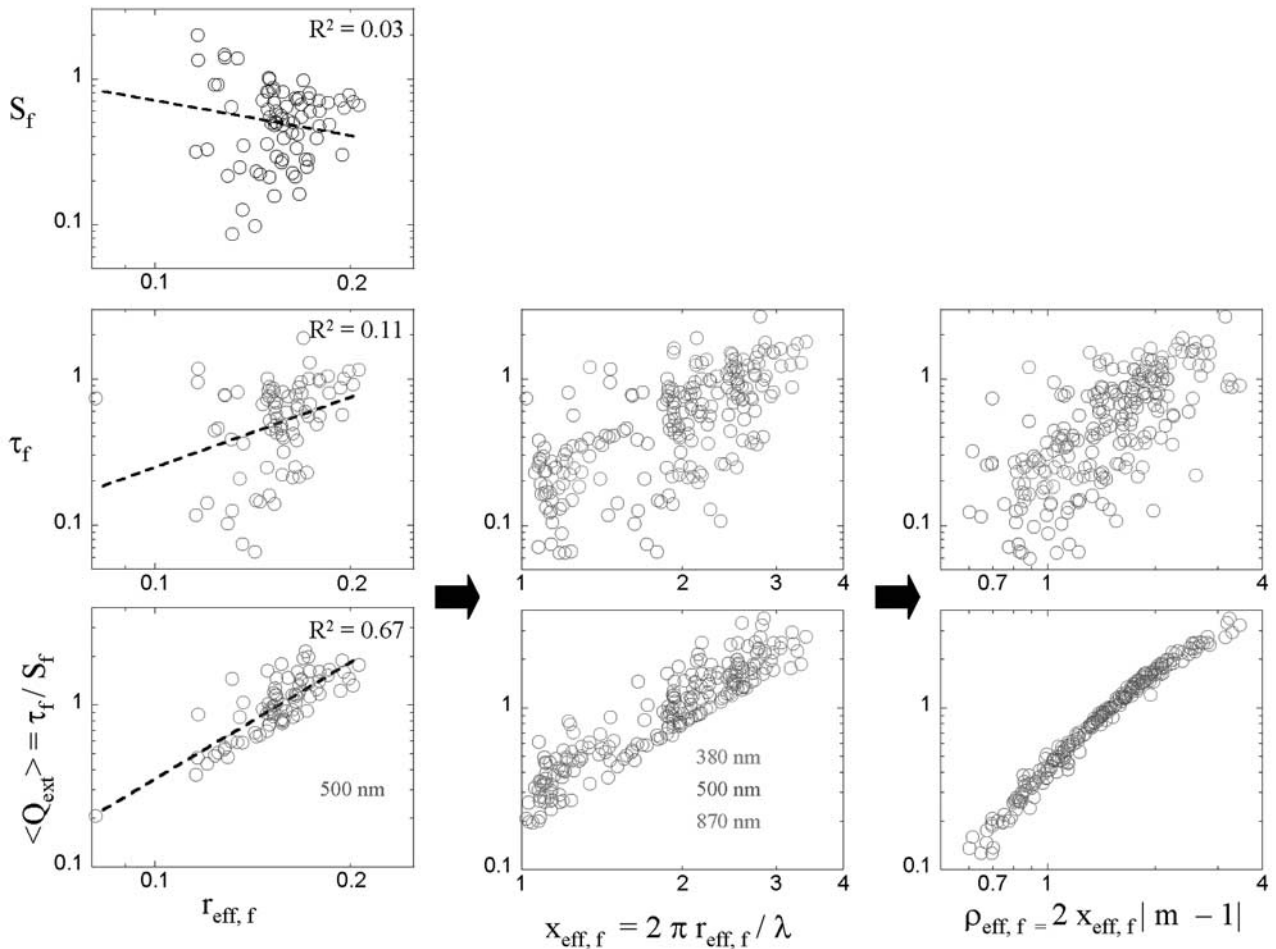


Figure 2a. Demonstration of the approach to a nearly monotonic dependence of $\langle Q_{\text{ext}} \rangle = \tau_f / S_f$ on $\rho_{\text{eff},f}$ for a representative data set (extracted from or computed from AERONET inversion data from Norfolk, VA, during July of 2002). The first column of graphs (vs $r_{\text{eff},f}$) are restricted to computations at 500 nm while the 2nd and 3rd column of graphs (vs $x_{\text{eff},f}$ and $\rho_{\text{eff},f}$ respectively) are plotted for 380, 500 and 870 nm. See color version of this figure at back of this issue.

slope of the bottom right-hand curve in Figure 2a should be a measure of the fine mode Angstrom exponent (note that this expression, and the Angstrom exponent in general, is independent of whether one uses \ln or \log). Figure 2b shows this explicitly: we have plotted the average of α_f , derived from fitting a second order spectral polynomial to the fine mode optical depth spectra obtained from the AERONET inversion, as a function of the value of α_f obtained from equation (2) (see the processing section for more details on the second order spectral polynomial). In order to obtain two points per wavelength we divided the ensemble of data points into two regimes of small and large $r_{\text{eff},f}$ (see figure caption for details).

[12] Another important LTPSD relation derived in Appendix B is the component contributions to the fine mode optical depth, viz:

$$\frac{d \log \tau_f}{d \log r_{\text{eff},f}} \approx \alpha_f + 2 + \gamma \quad (4)$$

$$\text{where } \gamma = \frac{d \log A_f}{d \log r_{\text{eff},f}}$$

and where A_f is the columnar fine-mode abundance (vertically integrated number density). The parameter γ can theoretically vary from $-\infty$ to $+\infty$ with notable values being -3 (conservation of volume), 0 (pure size-induced optical variations) and $\pm\infty$ (pure abundance variation). Equation (4) is instructive; it states that the variation of $\log \tau_f$ relative to $\log r_{\text{eff},f}$ is composed of (1) a purely particle size/particle type (intensive) influence of $\alpha_f + 2$ and (2) a purely mechanical influence associated with (extensive) abundance variations. This log ratio is perhaps more easily understood if one recalls that $d \log A_f / d \log r_{\text{eff},f} \approx (\Delta A_f / A_f) / (\Delta r_{\text{eff},f} / r_{\text{eff},f})$. Given that $\alpha_f \sim 1$ to 2 at 500 nm then an increase in $r_{\text{eff},f}$ will usually produce a positive increase in τ_f unless γ is strongly negative. The value of γ also embodies the influence of concentration dependent particle growth mechanisms such as coagulation and condensation.

2.2. Iso-Lines of Constant $\rho_{\text{eff},f}$

[13] Equation (3) formally describes the α'_f vs α_f curves of Figure 1 for a fine mode LTPSD (curves of constant geometric standard deviation for the log-normal PSDs which were used to generate the graph). The lines of

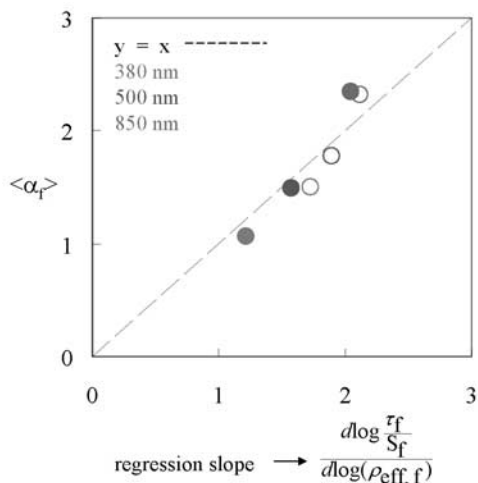


Figure 2b. Average value of α_f (extracted by fitting a second order polynomial to the AERONET inversion value of τ_f) as a function of α_f extracted from the regression slope of the τ_f/S_f versus $\rho_{\text{eff},f}$ points in Figure 2a. The two points per wavelength result from dividing the AOD data into regimes of $r_{\text{eff},f} < 0.159$ (open circular symbols) and $r_{\text{eff},f} > 0.159 \mu\text{m}$ (solid circular symbols). The cutoff of $0.159 \mu\text{m}$ represents the average value of $r_{\text{eff},f}$ for the ensemble of Norfolk, July 2002 data. See color version of this figure at back of this issue.

constant $\rho_{\text{eff},f}$ seen in the same figure are nearly orthogonal to these curves and approximately dependent on only α'_f vs α_f (i.e. independent of PSD width and refractive index). In point of fact we were able to derive an empirical relationship between $\rho_{\text{eff},f}$, α_f and α'_f over a comprehensive range of log-normal PSDs and refractive indices, viz;

$$\frac{\rho_{\text{eff},f}}{\rho_p} = a\psi^3 + b\psi^2 + c\psi + d \quad (5)$$

$$\tan \psi = \frac{\alpha'_f - \alpha'_{f,0}}{\alpha_f - \alpha_{f,0}},$$

where $\rho_p = 0.29$ is the value of $\rho_{\text{eff},f}$ at the anomalous diffraction peak (see Figure 1) and $(a, b, c, d) = (1.493\text{e-}6, 3.259\text{e-}4, 7.528\text{e-}3, 0.3676)$. ψ (in degrees) is the angle from the α_f axis subtended by a line of constant $\rho_{\text{eff},f}$ (all the lines of constant $\rho_{\text{eff},f}$ tend towards an approximate origin of $(\alpha_{f,0}, \alpha'_{f,0}) = (0.5, 0.2)$). The log-normal fine mode PSDs employed in generating this relationship included the biomass burning cases described in the caption of Figure 1 (with the PSD geometric standard deviation varying, additionally, from 1.5 to 1.8) as well as a set of more continental PSDs with geometric standard deviations varying from 1.5 to 1.8, real refractive index varying from 1.33 to 1.5 and complex refractive index varying from 0.0 to 0.004. The accuracy of equation (5) (relative rms errors of 13% and 4% for the biomass burning and continental cases respectively) serves again to confirm the strong monotonic dependence on $\rho_{\text{eff},f}$ but without the near-LTPSD condition imposed on equations (2) and (3). It also yields a convenient expression for $\rho_{\text{eff},f}$ which clarifies the universally accepted

paradigm that indicators of average particle size such as $r_{\text{eff},f}$ vary inversely with Angstrom exponent.

[14] Figure 3 shows the results of applying equation (5) to the Norfolk data. We did not investigate the scatter of the points beyond noting that a significant portion of the variation in the AERONET values of $\rho_{\text{eff},f}$ was induced through the $|m - 1|$ factor and that this factor was often characterized by somewhat improbable high-frequency diurnal variations.

[15] Finally we would re-emphasize that equations (2) to (5) were developed for the specific case of fine mode particles. In order to employ these equations as a basis of analysis one must either have a dominant fine mode event, fine mode optical parameters from AERONET inversions or a spectral deconvolution algorithm as presented in *O'Neill et al.* [2003]. The latter option will be the focus of future investigations.

3. Experimental Methodology

3.1. Processing of the Sunphotometer Data

[16] Sunphotometer data were acquired from the 10 stations employed in the analysis of the Québec smoke event (Table 1). Spectral curvature parameters at 500 nm were computed after applying a second order spectral polynomial [*Eck et al.*, 1999] to six of the CIMEL's seven channels (380, 440, 500, 670, 870, 1020 nm as per *O'Neill et al.* [2003]). Level 1.0 (non-cloud-screened) data were used in order to ensure that legitimate smoke data were not removed by the automated cloud screening process normally applied to AERONET data [*Smirnov et al.*, 2000]. The automated AERONET cloud screening procedure was designed to eliminate large temporal changes in optical depth: the creators opted not to apply an Angstrom exponent type of filtering criterion because it might eliminate legitimate dust data. This means that large variations in optical depth due to smoke events are occasionally filtered out.

[17] In lieu of the cloud screening algorithm (used to produce level 1.5 data) we carefully monitored the AOD and Angstrom exponent data sets for obvious cloud contamination and compared this with AVHRR animations to support our conclusions on the presence or absence of cloud. The AERONET level 2.0 processing chain provides data which are quality-assured and which are recalibrated based on pre and post comparisons with master reference instru-

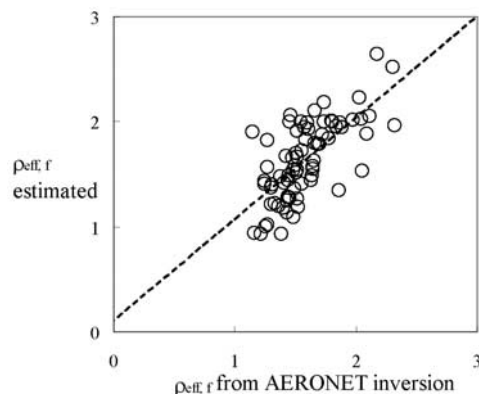


Figure 3. Estimated $r_{\text{eff},f}$ from equation (5) versus the values of $r_{\text{eff},f}$ from the AERONET inversion.

Table 1. AERONET/AEROCAN Sites Employed in the Québec Smoke Analysis^a

Station	Latitude, °N	Longitude, °W	Nominal Elevation, m	Distance to Source, km	Maximum AOD ^b (500 nm)
Howland, ME	45.200	68.733	100	900	1.3
Egbert, Ont.	44.226	79.750	264	950	1.8
Halifax, NS	44.638	63.594	65	1250	1.6
CCNY, NY	40.821	73.949	100	1250	2.1
MDSC, MD	39.283	76.617	15	1400	2.0
GSFC, MD	39.030	76.880	50	1450	1.8
SERC, VA	38.883	76.500	10	1500	2.0
Wallops Island, VA	37.942	75.475	10	1550	1.3
Norfolk, VA	36.848	76.259	20	1650	1.4
Cove, VA	36.900	75.710	0	1700	1.7

^aSmoke AODs were observed over one or more of these stations during the July 6 to July 10 Québec smoke event.

^bMaximum of AOD half-day averages (i.e. averages across the 6 hour trajectory average window).

ments. The level 2.0 optical depth uncertainty is ~ 0.01 to 0.015 with higher values for the 380 nm channel [Eck *et al.*, 1999]. In lieu of the level 1.5 to 2.0 QA and calibration step we opted to perform similar quality assurance checks on the level 1.0 data and to simply ensure that no large optical parameter differences existed between the measurements common to level 1.0 and level 2.0 data. We found that rms differences, during the Québec smoke event, were less than 0.007 for AOD, 0.06 for α and 0.14 for α' . For one station with calibration drift (CCNY), the corresponding rms errors were 0.025 , 0.024 and 0.17 respectively.

[18] The AERONET outputs from formal inversions of extinction and (almucanter) sky radiance data [Dubovik and King, 2000] were used as a reference source to better understand the spectral variations seen in the AOD data. In spite of the extreme utility of the inversion products, the reader should bear in mind that this data is very much undersampled relative to the spectral AOD data (there are 5 to 10 times more AOD samples than combined AOD and sky radiance samples). We further note that the level 1.5 AERONET inversion data were used for reasons similar to those stated above for the extinction data (and because the processing from level 1.5 to level 2.0 significantly reduced the already small number of points available from the level 1.5 database).

[19] Automated rejection filters based on signal magnitude in the 500 nm channel were deactivated so that we could obtain a more comprehensive picture of the smoke dynamics (at low signal levels or high values of slant optical depth). These filters were not conceived for the unprecedented types of conditions encountered during the Québec event and we opted to apply our own filters after observing the nominal AODs in each channel. In particular it became clear that low count problems for the largest AODs induced differential wavelength-dependent underestimates and artificially low Angstrom parameter values. We accordingly applied minimum-signal suppression filters to all wavelengths as part of our modified processing chain.

[20] The fine mode parameters of τ_f , α_f and α'_f employed in the preceding section were referenced to a single wavelength by applying a second order polynomial to all AOD spectra [O'Neill *et al.*, 2003]. These fine mode components (which all correspond to the limited data set of corresponding sunphotometer and sky radiance measurements) were obtained from the fine mode AODs which are the product of the AERONET inversion. For the Québec smoke

data we employed the total AOD spectra as indicators of fine mode behavior (the dominant smoke AODs permit one to assume that $\tau_f \cong \tau_a$, $\alpha_f \cong \alpha$, etc.).

3.2. Trajectory Times

[21] The HYSPLIT [Draxler and Rolph, 2003] back-trajectory algorithm (EDAS analyzed met. data) combined with observations of temporal and spectral AOD behavior at each station, GOES animations, MPLNet data [Welton *et al.*, 2001] and source position/duration estimates [Reid *et al.*, 2004] were employed to arrive at smoke particle trajectory times. Smoke-event time windows of 6 hours or less were first established by manually searching for cases of high AODs associated with stable and high Angstrom exponents during the July 6 to July 10 period when at least one of the stations was determined to be affected by smoke. The mid-time of these windows was then employed to initiate a backtrajectory run at 1500, 2500 and 3500 meters. This range of altitudes coarsely bracketed what information was available on plume height during the Québec smoke event [Colarco *et al.*, 2004; Taubman *et al.*, 2004]. If any of the backtrajectory traces crossed over a source region within the relatively narrow time windows when the sources were known to be strongly active [Colarco *et al.*, 2004] then that trace was labeled as acceptable and its nominal trajectory time was recorded. There are, of course, large uncertainties in these estimates related to the effective temporal and spatial resolution of the analyzed wind fields, the lack of knowledge of the plume altitude, uncertainties in the precise location of the emission sources and the graphical method used to estimate the trajectory times. We estimated these uncertainties to be between 6 and 9 hours for the smaller trajectory times and from 6 to 15 hours for the larger trajectory times. When available, MPLNet vertical profile information of aerosol backscatter at GSFC [Welton *et al.*, 2001] was employed for the central east-coast sites to reduce uncertainties in trajectory times due to uncertainties in smoke height (i.e. to eliminate the trajectory times at specific altitudes). Finally we note that all optical and $r_{\text{eff},f}$ data reported below were averaged over the smoke-event time windows.

4. Experimental Conditions

[22] Most of those events whose trajectory time could be satisfactorily verified were traceable to a window of approximately 0900 to 2100 GMT on July 5 [cf. Colarco

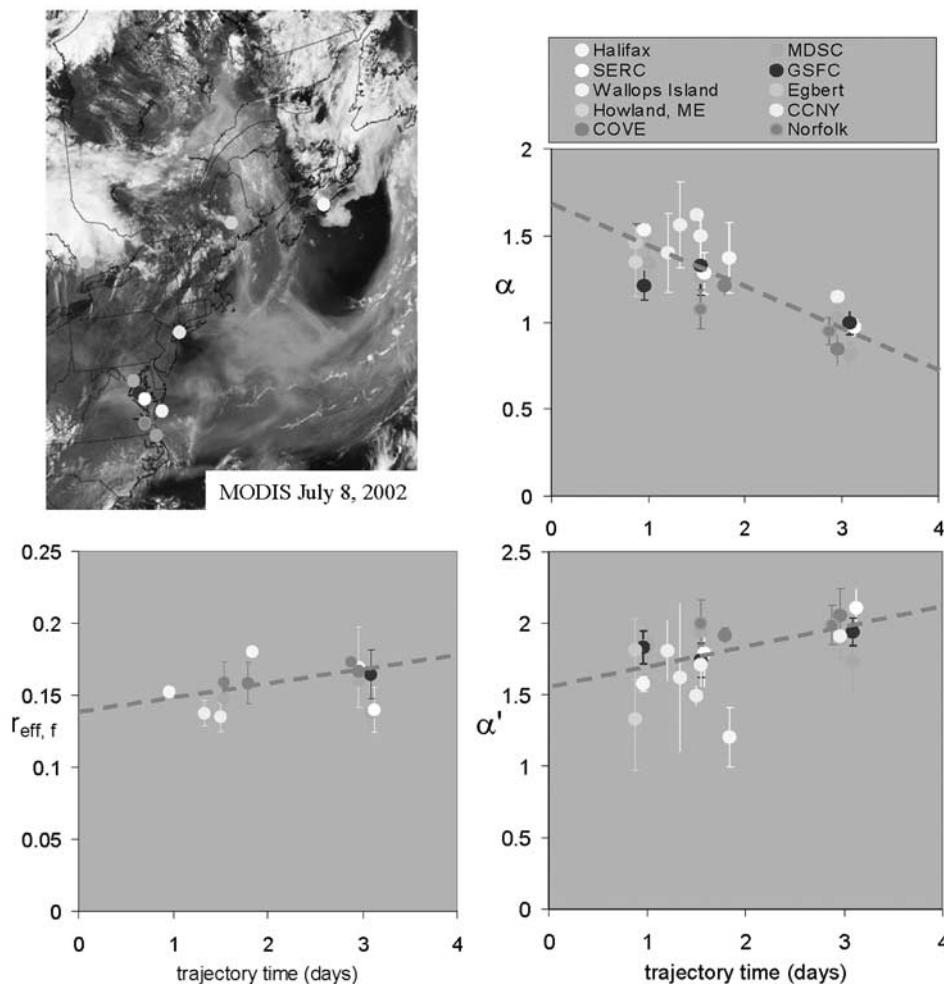


Figure 4. Sample MODIS image along with graphs of α , α' and $r_{\text{eff},f}$ as a function of trajectory time (t) for all sunphotometer sites where data were acquired during the Québec smoke event (see Table 1 for site data). α and α' were computed at the reference wavelength of 500 nm. The red markings on the MODIS image show fire source locations. The grey dashed lines represent overall regression lines. Each point and its error bar is an average and standard deviation of all sunphotometry data acquired for ± 6 hours on either side of the nominal trajectory arrival time. The $r_{\text{eff},f}$ versus t graph has fewer points than the α versus t and the α' versus t graphs because not all extinction measurement time windows encompassed an inversion time. In addition each point of the $r_{\text{eff},f}$ versus t graph represents fewer measurements since inversions were relatively rare (see Table 2). See color version of this figure at back of this issue.

et al., 2004]. Essentially the smoke released by the July 5th sources was observed at Egbert and CCNY on July 6th and over the central east-coast sites throughout July 7. In the latter case, GOES animations confirmed that a cloud band was interspersed with and thus contaminating the smoke signature with high temporal frequency variations in AOD and Angstrom exponent on the afternoon of July 7th. The smoke plume was then constrained by local circulation and continued to persist over the central east coast sites throughout July 8th and July 9th. On the morning of July 9th the backtrajectories once again were traced to emissions on July 5th but the AOD and Angstrom exponent variations were of sufficiently high frequency to indicate interspersed cloud effects: this data were accordingly not employed in the analysis. Only CCNY, Howland, ME and Halifax, NS were associated with different source windows (0900–

2100 GMT on July 6th for CCNY, 1700–0030 GMT, July 7 for Howland and 1700–0030 GMT, July 7 as well as 1415–2230, July 8 for Halifax).

5. Systematic Features Versus Trajectory Time

[23] Figure 4 shows multi-station results of α , α' and $r_{\text{eff},f}$ vs trajectory time for the Québec smoke event (where each point and its error bar represent an average and standard deviation across the 6 hour time window discussed above). The $r_{\text{eff},f}$ points were derived from the fine mode distribution of the AERONET inversions: there are fewer $r_{\text{eff},f}$ points (and each point represents significantly fewer measurement samples) since combined almucantar/extinction measurements are relatively rare. While the trends are fair to marginal in terms of statistical significance they are sys-

Table 2. Trend Statistics for the Variation of α and α' (at 500 nm Wavelength) and $r_{\text{eff},f}$ With Trajectory Time (for the Points of Figure 4)^a

	α Versus Trajectory Time			α' Versus Trajectory Time			$r_{\text{eff},f}$ Versus Trajectory Time		
	Slope, days ⁻¹	R ²	N	Slope, days ⁻¹	R ²	N	Slope, $\mu\text{m}/\text{day}$	R ²	N
Québec smoke	-0.226	0.66	361	0.128	0.23	361	0.0034	0.04	36

^aN is the total number of measurements that were employed in creating the points of Figure 4 (i.e. each point being an average of ± 6 hours of data about the nominal trajectory arrival time).

tematically coherent in that they indicate a particle size increase with trajectory time. Similar trends were found in [O'Neill *et al.*, 2002] versus trajectory distance (and in a later calculation versus trajectory times). Table 2 shows the regression statistics for the trends of Figure 4 (including the total number of samples which were employed to create the averaged points of the figure: the value of N in the case of the $r_{\text{eff},f}$ points being approximately 1/10 of the value for the α and α' points).

[24] The average $r_{\text{eff},f}$ growth rate of about 0.0034 $\mu\text{m}/\text{day}$ in Table 2 is significantly below the regional growth rates of the order of 0.01 $\mu\text{m}/\text{day}$ given by Reid *et al.* [1998] and inconsistent (given an assumption of a uni-modal fine mode) with the α and α' variation for the Québec smoke (see below). It is also at odds, given a hypothesis that coagulation and/or condensation effects were significant, with the large AODs (and by inference large particle concentrations) present in the Québec smoke plumes. Reid *et al.* [1998] have argued that particle growth trends in Brazilian smoke were significantly influenced by condensation over periods of the order of a few hours and condensation and coagulation effects over periods of the order of a few days. Colarco *et al.* [2004], in fact, employed simulations of the Québec smoke event to argue that coagulation was a significant cause of particle growth effects observed in AERONET inversions at the GSFC site (other mechanisms such as condensation were not considered). These results suggest that the low growth rate of $r_{\text{eff},f}$ observed in Figure 4 is an anomaly which requires further investigation (see the following section).

[25] The presence of enhanced NO₂ in smoke plumes [see, e.g., Thomas *et al.*, 1998] and the fact that NO₂ absorption mimics the presence of smaller aerosol particles [Shaw, 1976] was likely not a factor in this analysis. GOME estimates of NO₂ abundance showed a maximum of less than 20×10^{15} molecules/cm² or less than approximately 0.01 in NO₂ optical depth for the CIMEL bands susceptible to the most significant NO₂ absorption (340, 380, 440 and 500 nm bands). These levels are insignificant relative to the measured smoke optical depths at 500 nm (all greater than 0.5). This conclusion still holds if one accounts for the aerosol corrections to GOME estimates outlined by Martin *et al.* [2003] (the corrected NO₂ optical depths only increase by about a factor of 2). Similar GOME based computations for ozone effects indicated that ozone optical depth enhancements due to smoke were also insignificant.

6. Optical and Physical Interpretations

6.1. Interpretation of the α' Versus α Diagram

[26] Eck *et al.* [2001] first noted systematic variations in measured values of α and α' and observed that the latter parameter is significantly more dependent on the absorptive property of the aerosol particles. Figure 5 shows the variation of α' versus α for all averaged data shown in

Figure 4. The α'_f versus α_f Mie curves of constant geometric standard deviation as well as the lines of constant $r_{\text{eff},f}$ of Figure 1 are superimposed in order to give some theoretical (uni-modal) context to the observed co-variance (we can speak of $r_{\text{eff},f}$ rather than $\rho_{\text{eff},f}$ because the $|\text{m} - 1|$ change between the three curves is very small). Particle size is the greater influence on the observed trend with the cluster of points straddling iso- $r_{\text{eff},f}$ lines ranging from 0.10 to 0.23 μm . The points vary between two extremes of weakly absorbing large particles and/or narrow-PSD (low α , high α') to more strongly absorbing small particles and/or broader-PSD (high α , low α'). It is noted that the single scattering albedo (SSA) from the AERONET inversion showed no correlation with trajectory time and thus no distinct pattern on the α' versus α graph could be associated with the retrieved values of SSA. Given the small number of SSA retrieval samples as well as their large nominal uncertainty relative to the range of retrieved values (± 0.03 as per Dubovik *et al.* [2000]) versus 0.05) we feel that this retrieval product must be treated with a fair amount of caution.

6.2. Apparent Inconsistencies in the α' Versus α Diagram and Their Physical Implication

[27] The high α' values in the (low α , high α') region of Figure 5 imply (with respect to a uni-modal fine mode PSD) that $r_{\text{eff},f}$ is significantly larger than the $r_{\text{eff},f}$ predicted from the AERONET inversion. This is because of an asymmetric tail of moderate to marginal optical importance found in many of the inverted fine mode distributions (see the illustration in Figure 6a). This tail acts to broaden the AERONET-derived fine mode standard deviation towards the lower-end particle sizes at the expense of a significantly less dramatic increase in $r_{\text{eff},f}$. The larger mode of a bi-modal fit to the asymmetric size distribution is much more monodisperse and yields an $r_{\text{eff},f}$ which is more coherent with the spectral curvature results; this is because the effective radius is a purely mechanical calculation and accordingly the mechanical weight of the asymmetric wing significantly exceeds its optical weight (in point of fact, Hansen and Travis [1974] defined the effective radius as a pragmatic approximation to an optically weighted effective radius). Eck *et al.* [2001] observed a similar asymmetric tail phenomenon in Zambian smoke data and demonstrated a strong correlation between the peak of the retrieved fine mode PSD and the AOD (subsequent computations with the data of Eck *et al.* [2001] indicated a similar strong correlation with the effective radius of the larger mode while the effective radius of the total asymmetric fine-mode PSD showed little correlation with AOD).

[28] While the asymmetric tail of the inverted fine mode PSD is not optically insignificant, we have found, for all the optical and physical computations performed in this paper, that it is systematically more appropriate to use the larger fine-mode PSD feature and its optical properties as representative of smoke properties during the Québec event. The

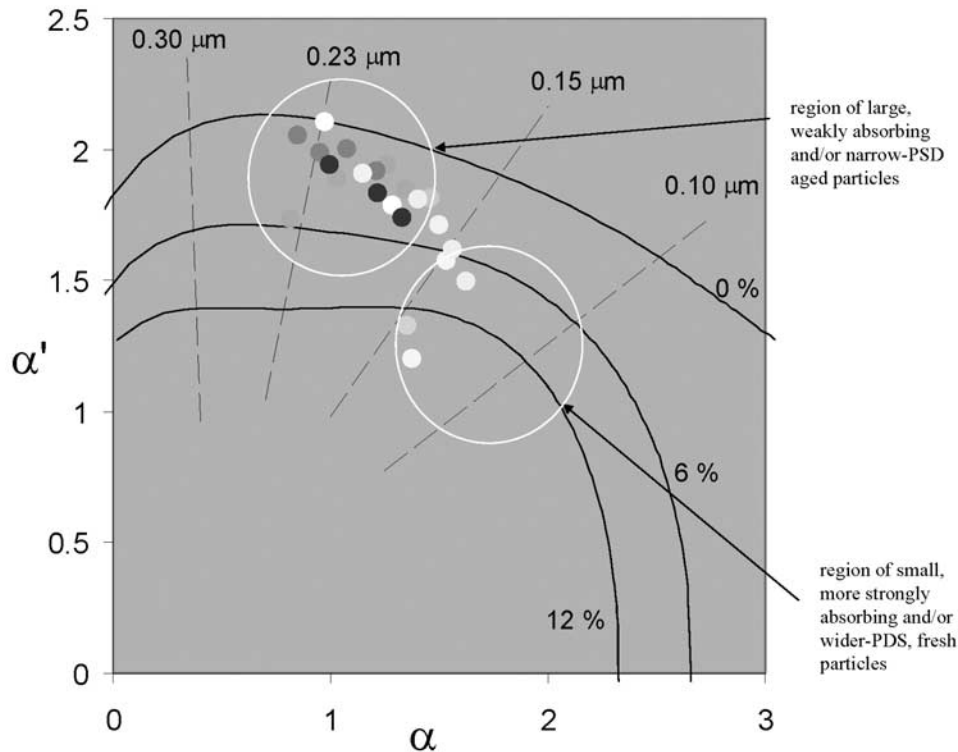


Figure 5. α' vs α for the Québec smoke event (same station colors and symbols as for Figure 4). Superimposed on the data are the simulated Mie curves defined in the caption of Figure 1. See color version of this figure at back of this issue.

source of the tail, whether a real aerosol particle feature or some form of systematic retrieval artifact, is difficult to determine with certainty. Although its consistent appearance in the inversion results of most of the station-data sampled during the Québec smoke events would appear to rule out both instrumental and inversion artifacts, the PSD variations from one inversion sample to the next could be quite significant (with little or no associated variations in the spectral form of the AOD data). Conversely, the multi-altitude airborne measurements of *Taubman et al.* [2004] made on July 8, 2002 over sites in Maryland and Virginia indicated the presence of low-lying smaller-particle pollution that was below the distinct smoke layer attributed to the Québec fires. The AOD contribution of this pollution layer is of the order of the AOD values of the asymmetric tails observed in our data. As well, the asymmetric tails appeared only in the inversion results of the turbid southern stations: such tails were absent or very much weaker in the Halifax and CCNY inversions.

[29] In order to render α and α' more coherent with the optical notion of effective radius we applied bi-modal log-normal fits to the AERONET inversions and computed the effective radius of the more optically significant larger-radius mode (see Figure 6a for an illustration of the fit). This modified effective radius ($r_{\text{eff},f,2}$) was strongly correlated with the modal radius of the larger-radius mode (because of the nature of the log-normal fit). The trajectory time dependence of $r_{\text{eff},f,2}$ is compared with the original $r_{\text{eff},f}$ values in Figure 6a. Its range of values is (as expected) more coherent with the range of values between the iso-lines of constant $r_{\text{eff},f}$ in Figure 5. The trend statistics for $r_{\text{eff},f,2}$ are a

slope of $0.034 \mu\text{m}$ per day and $R^2 = 0.57$ (versus 0.003 and 0.04 respectively for $r_{\text{eff},f}$). By comparison we computed the coagulation coefficient using time-averaged log-normal parameters from the peak 2 computations of Figure 6a for all the Québec smoke data and assuming conservation of volume (equations (2) and (3) of *Reid et al.* [1998]). In such a case one finds that the rate of increase of the average fine mode particle volume is given by

$$\frac{dv_f}{dt} = v_{f,0} N_{f,0} K \quad (6)$$

where $N_{f,0}$ is the initial fine mode number density, K is the coagulation coefficient and $v_{f,0}$ is the initial fine-mode particle volume. Assuming a full width at half maximum (FWHM) plume thickness of $\Delta z \sim 500 \text{ m}$ [*Taubman et al.*, 2004] and thus a plume number density, $N_{f,0} \sim A_f/\Delta z$, one finds a rate of volume increase of $\sim 0.01 \mu\text{m}^3/\text{day}$ which corresponds to an average $r_{\text{eff},f,2}$ rate of $\sim 0.03 \mu\text{m}/\text{day}$. This close agreement with the $0.034 \mu\text{m}/\text{day}$ ($r_{\text{eff},f,2}$) case above is fortuitous to an extent since (for example) the assumed thickness of the smoke layer might well be significantly different from the few examples extracted from *Taubman et al.* [2004]. With respect to the conservation of volume assumption, Figure 6b shows that the dependence of the fine mode abundance for the peak 2 case of Figure 6a yields a slope (γ) close to -3 (this is approximately coherent with equation (4) where $d \log \tau_f / d \log r_{\text{eff},f,2} \cong 1.1$ and $\alpha_f \cong \langle \alpha \rangle = 1.2$ yields $\gamma = -2.2$). It is also noted that the intercept of Figure 6b was employed to estimate the $v_{f,0} N_{f,0}$ product of equation (6).

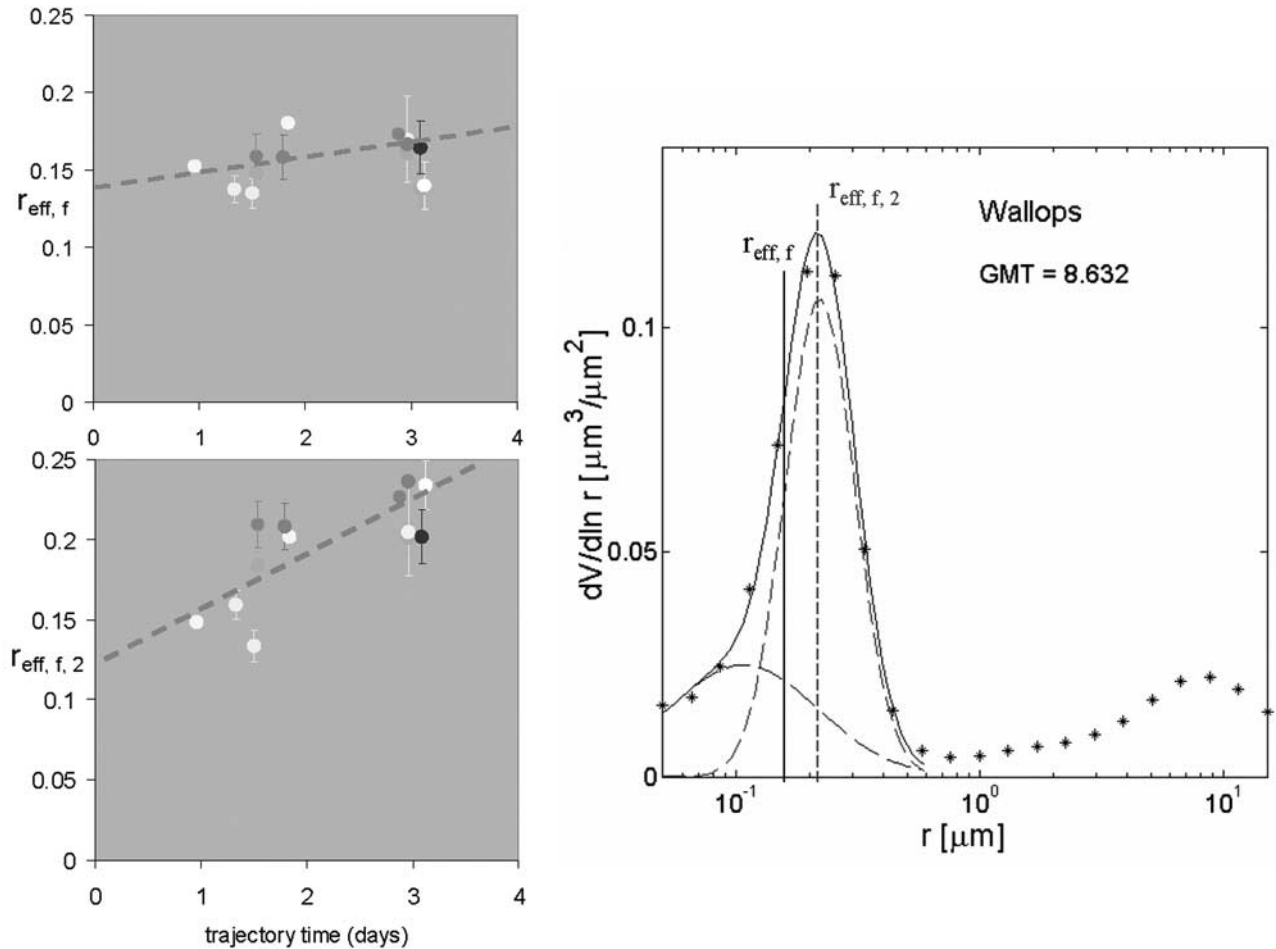


Figure 6a. Variation of $r_{\text{eff},f,2}$ (the effective radius of the larger-radius mode of the fine mode PSD) as a function of trajectory time, alongside the original variation of $r_{\text{eff},f}$ from Figure 4. The rightmost graph is an illustration of the bimodal fitting procedure which was applied to the AERONET inversion PSDs to yield $r_{\text{eff},f,2}$. In this latter figure the asterisks represent the data while the dashed curves represent the bimodal components of the total fitted (solid line) curve. See color version of this figure at back of this issue.

[30] The value of $\gamma = -3$ is by no means a characteristic result; the data of *Eck et al.* [2001] yielded $\gamma \sim 0$ (γ being computed from a $\log A_{f,2}$ vs $\log r_{\text{eff},f,2}$ regression as per Figure 6b). In this case $d \log \tau_f / d \log r_{\text{eff},f,2}$ at 440 nm was correspondingly large (~ 5). One could simply interpret these differences as an effectively closed system in the case of $\gamma = -3$ versus an unconserved open system in the Eck case of $\gamma \sim 0$.

[31] We note that solving for γ in equation (4) would yield a value of $\gamma \sim 1.4$ in the Eck case for an average α_f value of ~ 1.6 as per Figure 11 of *Eck et al.* [2001]. This difference ($\gamma \sim 0$ vs $\gamma \sim 1.4$) is likely attributable to the fact that positive correlation was found to exist between the retrieved value of $|m - 1|$ and $r_{\text{eff},f,2}$ (see equation (A8)); the basis for replacing $\log(\rho_{\text{eff},f})$ by $\log(r_{\text{eff},f})$ in the derivation of equation (4) is that $\log |m - 1|$ is approximately constant or at least uncorrelated with the effective radius).

[32] The geometric standard deviation of the peak 2 fine mode ($\sigma_{V,f,2}$) for the Québec smoke actually decreased slightly with trajectory time while the total fine-mode $\sigma_{V,f}$ of the AERONET inversion significantly increased with

trajectory time. Although the regression line in the former case was not significant, the negative slope tendency was more coherent with the results of *Reid et al.* [1998], who actually observed a decrease of $\sigma_{V,f}$ with aging. In point of fact, *Reid et al.* [1999] used the observed negative correlation to argue that condensation was a significant particle growth mechanism in smoke-dominated hazes over Brazil (as opposed to coagulation where the trend is expected to be neutral).

[33] Figure 6c shows a comparison between our estimates of $r_{\text{eff},f}$ using equation (5) and the $r_{\text{eff},f}$ and $r_{\text{eff},f,2}$ values from Figure 6a (using the AERONET inverted values of refractive index to transform $\rho_{\text{eff},f}$ of equation (5) to $r_{\text{eff},f}$). This graph once again confirms the monotonicity as a function of $\rho_{\text{eff},f}$ and in particular shows that $\rho_{\text{eff},f,2}$ or $r_{\text{eff},f,2}$ are coherent with single mode optics.

7. Universality of Observed Trends

[34] If the PSD is approximately log-translatable then one expects a nearly monotonic dependence of the measured

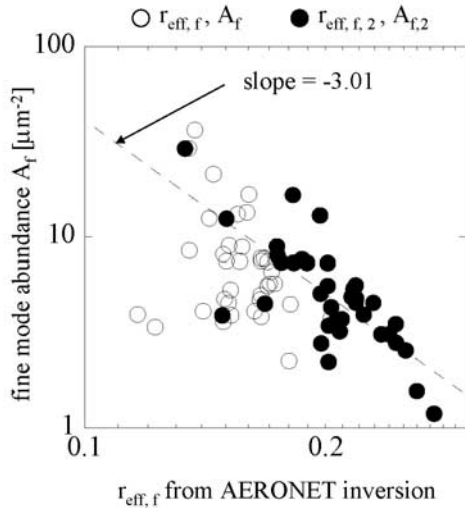


Figure 6b. Variation of the fine mode abundance as a function of effective radius for both cases of Figure 6a. The dashed line is the regression through the peak 2 ($r_{\text{eff},f,2}$, $A_{f,2}$) case.

spectral parameters α and α' on $\rho_{\text{eff},f}$. Figure 7 shows the variation of α at 380, 500 and 870 nm as a function of the inter-related variables of trajectory time (t), $r_{\text{eff},f}$ and $\rho_{\text{eff},f}$. The similarity between the α vs t and α vs $r_{\text{eff},f}$ graphs indicates that the time dependence is merely a proxy for $r_{\text{eff},f}$ which in turn is an incomplete manifestation of the more universal variable $\rho_{\text{eff},f}$. Given a logarithmic rate of $d \ln r_{\text{eff},f} / d \ln t \sim 0.4$ (which is the logarithmic analogue to the 0.034 $\mu\text{m}/\text{day}$ rate given above) then the slope of α versus $\ln t$ in terms of α versus $\ln r_{\text{eff},f}$ can be expressed as;

$$\left(\frac{\partial \alpha}{\partial \ln t} \right)_{\lambda} = \left(\frac{\partial \ln \rho_{\text{eff},f}}{\partial \ln t} \right)_{\lambda} \frac{d\alpha}{d \ln \rho_{\text{eff},f}} \\ \approx \frac{d \ln r_{\text{eff},f}}{d \ln t} \left(\frac{\partial \alpha}{\partial \ln r_{\text{eff},f}} \right)_{\lambda} \approx 0.4 \left(\frac{\partial \alpha}{\partial \ln r_{\text{eff},f}} \right)_{\lambda}$$

This expression does indeed approximately describe the relationship between the obviously correlated slopes of the first and second graphs of Figure 7.

[35] The approximately monotonic dependence of α on $\rho_{\text{eff},f}$ in the right-most graph is underscored by superimposing the solid-trace Mie curve from Figure 1. According to equation (3) the slope of this curve should yield α'_f or α' for the Québec cases of high AOD (and the regression lines should line up approximately with the solid Mie curve). The underestimate of the regression line slopes relative to the slope of the solid-trace Mie curve and relative to independent averages of α' is coherent with Figure 5 where five of the Québec smoke points (corresponding to short trajectory times) cross iso-lines of constant complex refractive index and/or geometric standard deviation towards the region of small, more strongly absorbing, fresh particles.

[36] The conflicting dependencies on size and number density make arguments of proxy variation complex when one examines the variation of α and α' with AOD as the dependent parameter. Reid *et al.* [1999] argued that the

AOD (at 498 nm) was essentially a proxy variable for median diameter in their Amazonian smoke data (the differences in α versus AOD slopes which they found between different wavelengths in their Figure 8 are coherent with our Figure 7 if one assumes that size effects dominate the AOD). However if the fine-mode abundance A_f is significantly anti-correlated with $r_{\text{eff},f}$ as was in the case for the Québec fires (whether or not one makes the peak 2 assumption of Figure 6a) then such arguments must be tempered by considerations of the relative contributions of $r_{\text{eff},f}$ (or $r_{\text{eff},f,2}$) and abundance (i.e. by the value of γ in equation (4)). The trends between α and AOD and α' and AOD were negative and positive respectively for the Québec smoke data. This suggests that the α and α' variations are analogous to the temporal trends of Figure 4 with the proviso that the (purely intensive) effective radius impact is reduced by negative γ (see Figure 6b and equation (4)).

8. Summary and Conclusions

[37] Simple relations between the fundamental fine mode parameters of τ_f , α_f , α'_f and $r_{\text{eff},f}$ were derived for the conceptual case of a log-translatable PSD (LTPSD). This simple formulation is to a certain degree applicable to the interpretation of real sunphotometer data because the fine mode size distribution often approximates a LTPSD in its behavior. At the same time, departures from this behavior are instructive in that second order perturbations become more readily understood once one understands the physics of the first order perturbations. The near monotonic dependency of the fine mode optical parameters on $\rho_{\text{eff},f}$ was also exploited to obtain an explicit expression for $\rho_{\text{eff},f}$ as a function of α_f and α'_f . The relations were applied to a representative case study to demonstrate their general applicability and then to the specific case of the July 2002 Québec smoke event. A number of illustrations were given where the coherency of the derived relations confirmed that the LTPSD concept was often a good approximation to reality.

[38] The analysis of the Québec smoke data showed the existence of a weak but systematic dependence of α and α' on smoke trajectory time and by inference a steady growth

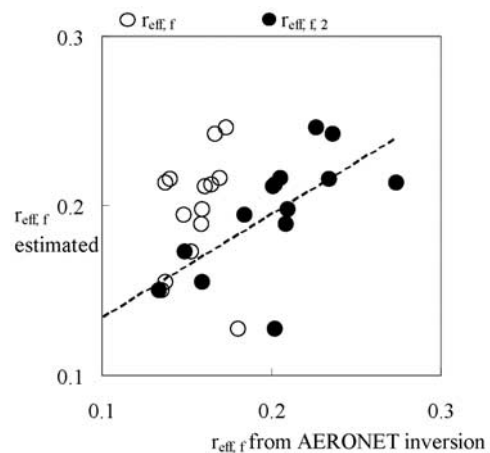


Figure 6c. Estimated $r_{\text{eff},f}$ from equation (5) vs the values of $r_{\text{eff},f}$ and $r_{\text{eff},f,2}$ from Figure 6a.

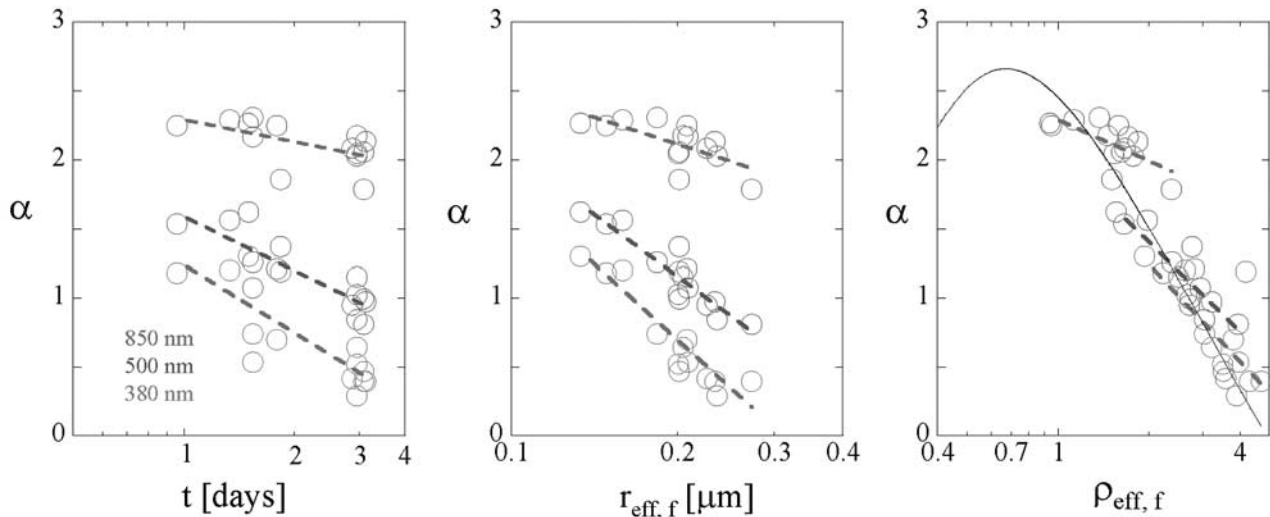


Figure 7. α vs trajectory time (t), $r_{\text{eff},f,2}$ and $\rho_{\text{eff},f,2}$ for the Québec smoke event data. The points are the result of the 6 hour averages which encompass the inversion times of the $r_{\text{eff},f}$ versus t graph of Figure 4 (the 500 nm points are a subset of the set of points seen on the α versus t graphs of Figure 4). See color version of this figure at back of this issue.

in particle size with time. The variation of $r_{\text{eff},f}$ was inconsistent with the variation of α and α' unless one redefined this essentially mono-modal parameter in terms of the clearly delineated peak of the asymmetric fine mode PSD (which seemed to be representative of the southern stations employed in the analysis). This definition led to a re-computed temporal rate of increase in $r_{\text{eff},f}$ which was consistent with the variation of the Angstrom parameters as well as with a simple coagulative model based on conservation of volume. It was demonstrated that trajectory time was essentially a proxy variable for $r_{\text{eff},f}$ and more fundamentally its optical representation $\rho_{\text{eff},f}$. A similar argument could be applied to the dependence of α on the AOD but such arguments are tempered by how the fine-mode abundance (A_f) varied with $r_{\text{eff},f}$ (by the value of γ). Finally it was suggested that the behavior of the slope α' on the graphs of α versus $\rho_{\text{eff},f}$ represented an instructive deviation from the LTPSD concept.

[39] Although these results appear to offer a reasonably coherent interpretation of the Québec smoke event in terms of the simple and robust equations presented in this paper, one must be ever mindful of the numerous simplifying assumptions which were made along the way. These include the transformation from point-volume optical and physical quantities to their vertically integrated analogues; the assumptions that fine mode PSD width and refractive index are of secondary importance in terms of their variation; and in general the treatment of a complex meteorological event in terms of crude, phenomenological, first order variables (such as the nominal trajectory time). *Reid et al.* [1998, 1999] pointed out other complicating factors such as the fact that particle sizes at the source were dependent on fire intensity; the influence of cloud processing on particle size and chemistry; and the influence of local chemistry on condensation and cloud processing mechanisms. The choice of the Québec smoke event as a test bed for the robustness of the LTPSD derived relations was, on the other hand, fortunate since this event was characterized by relatively

local and strong emission sources, by very strong AOD signals and by relatively simple meteorology.

Appendix A: Log-Translatable PSD (LTPSD)

[40] We define a log-translatable PSD (LTPSD) as a PSD whose normalized abundance only varies by a simple shift (translation) in log-space, viz;

$$\frac{1}{A'} \frac{dA'}{d \log r'} (\log r') = \frac{1}{A'} \frac{dA'}{d \log r'} (\log r + \log k) = \frac{1}{A} \frac{dA}{d \log r} (\log r) \quad (\text{A1})$$

With this definition in hand, the geometric mean and standard deviation of the translated PSD are respectively;

$$\begin{aligned} \log r'_A &= \int \log r' \frac{1}{A'} \frac{dA'}{d \log r'} (\log r') d \log r' \\ &= \int (\log r + \log k) \frac{1}{A} \frac{dA}{d \log r} (\log r) d \log r \\ &= \log r_A + \log k \end{aligned} \quad (\text{A2})$$

$$\begin{aligned} \log^2 \sigma'_A &= \int (\log r' - \log r'_A)^2 \frac{1}{A'} \frac{dA'}{d \log r'} (\log r') d \log r' \\ &= \int (\log r - \log r_A)^2 \frac{1}{A} \frac{dA}{d \log r} (\log r) d \log r \\ &= \log^2 \sigma_A \end{aligned} \quad (\text{A3})$$

The implications of the log-translatable properties on the cross-sectional surface PSD and the volume PSD are respectively;

$$\begin{aligned} \frac{dS'}{d \log r'} (\log r') &= \pi r^2 \frac{dA'}{d \log r'} (\log r') \\ &= k^2 \pi r^2 \frac{dA}{d \log r} (\log r) = k^2 \frac{dS}{d \log r} (\log r) \end{aligned}$$

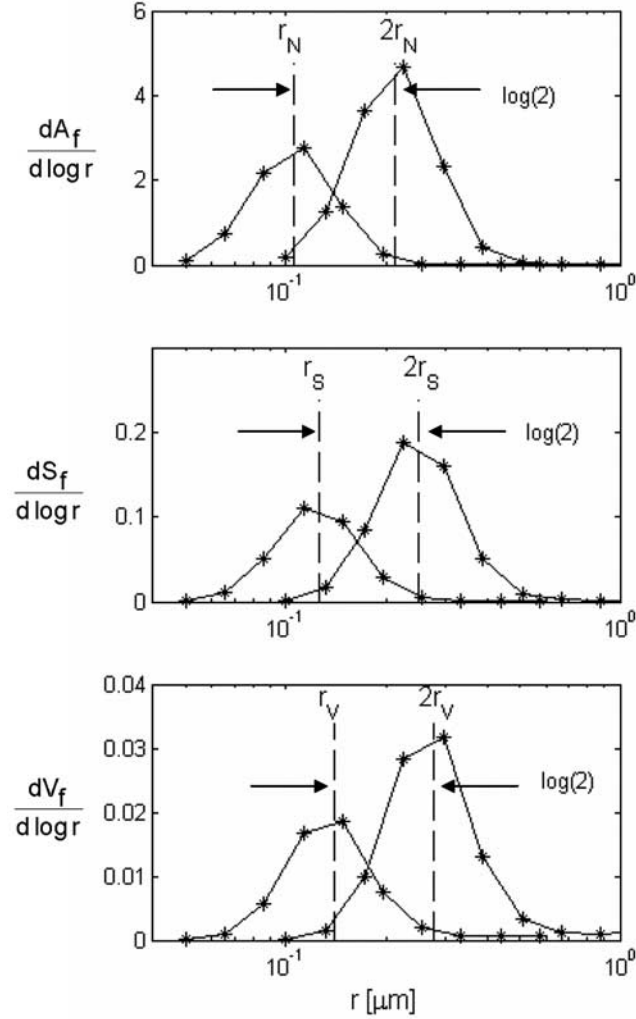


Figure A1. Abundance (integrated number density), cross-sectional surface and volume PSDs for the case of a LTPSD (log-translatable PSD). In this example the left hand PSD goes through a 70% increase in total abundance and a multiplicative increase of a factor of 2 in all particle radii (shift of $\log(2)$ on the $\log r$ axis). The units of $dA/d\log r$, $dS/d\log r$ and $dV/d\log r$ are μm^{-2} , $\mu\text{m}^2/\mu\text{m}^2$, and $\mu\text{m}^3/\mu\text{m}^2$ respectively. The abundances employed to initialize these computations were taken from a sample AERONET inversion.

$$S' = k^2 S \text{ and thus } \frac{1}{S'} \frac{dS'}{d\log r'}(\log r') = \frac{1}{S} \frac{dS}{d\log r}(\log r)$$

$$\begin{aligned} \frac{dV'}{d\log r'}(\log r') &= \frac{4}{3} \pi r'^3 \frac{dA'}{d\log r'}(\log r') = k^2 \frac{4}{3} \pi r^3 \frac{dA}{d\log r}(\log r) \\ &= k^2 \frac{dV}{d\log r}(\log r) \end{aligned}$$

$$V' = k^3 V \text{ and thus } \frac{1}{V'} \frac{dV'}{d\log r'}(\log r') = \frac{1}{V} \frac{dV}{d\log r}(\log r)$$

which means that if the abundance is log translatable then the surface and volume PSDs are also log translatable. It follows (as for the abundance PSD) that;

$$\log r'_S = \log r_S + \log k \text{ and } \log r'_V = \log r_V + \log k \quad (\text{A4})$$

$$\log^2 \sigma'_S = \log^2 \sigma_S \text{ and } \log^2 \sigma'_V = \log^2 \sigma_V \quad (\text{A5})$$

The effective radius of *Hansen and Travis* [1974] is also a simple logarithmic translation, viz;

$$r'_{\text{eff}} = \frac{\int r'^3 \frac{dA'}{d\log r'} d\log r'}{\int r'^2 \frac{dA'}{d\log r'} d\log r'} = \frac{k^3 \int r^3 \frac{dA}{d\log r} d\log r}{k^2 \int r^2 \frac{dA}{d\log r} d\log r} = k r_{\text{eff}}$$

Such parameters thus translate with the LTPSD and can effectively be thought of as being fixed relative to the LTPSD.

[41] Finally we note that the definition of the LTPSD can be rendered more succinct. If r_A^* , r_S^* and r_V^* are radii attached to the abundance, surface and volume LTPSDs respectively then the normalized representations are functions of the relative distance from these characteristic radii, viz;

$$\begin{aligned} \frac{1}{A} \frac{dA}{d\log r} &= \hat{a}(\log r - \log r_A^*), \quad \frac{1}{S} \frac{dS}{d\log r} = \hat{s}(\log r - \log r_S^*), \text{ and} \\ \frac{1}{V} \frac{dV}{d\log r} &= \hat{v}(\log r - \log r_V^*) \end{aligned} \quad (\text{A6})$$

Stated otherwise, the normalized LTPSDs are invariant as long as the relative distance from any PSD feature remains fixed.

[42] Figure A1 shows an example of a fine mode LTPSD where the simulated change from the left hand PSDs to the right hand PSDs involves (a) a simple log translation corresponding to a factor of two increase in particle size and (b) a bulk abundance increase of 70%. The figure illustrates how the LTPSD (in each of the three cases) retains its form while being log-translated to the right (as per equation (A1) for example).

Appendix B: Derivation of Effective Mie Relations

B1. Implication of a Log-Translatable PSD (LTPSD)

[43] The Mie extinction cross section can be written as the average (over $\log r$);

$$\begin{aligned} \langle C_{\text{ext}} \rangle(m, \lambda, \bar{x}) &= \frac{\tau_f}{A_f} \\ &= \frac{1}{A_f} \int_{-\infty}^{\infty} Q_{\text{ext}}(m, r, \lambda) \frac{dS_f}{d\log r}(\log r, \bar{x}) d\log r \end{aligned} \quad (\text{B1})$$

where $\frac{dS_f}{d \log r}(\log r, \vec{x}) = \pi r^2 \frac{dA_f}{d \log r}(\log r, \vec{x})$ is the cross-sectional surface PSD, r is the particle radius, $\frac{dA_f}{d \log r}(r, \vec{x})$ is the abundance (vertically integrated number density) PSD, \vec{x} is a vector of PSD descriptor parameters, m is the complex refractive index, $C_{\text{ext}}(m, r, \lambda)$ is the extinction cross section and $Q = \frac{C_{\text{ext}}(m, r, \lambda)}{\pi r^2}$ is the extinction efficiency (implicitly averaged over altitude).

[44] If one defines the average cross-sectional area as $s_f = S_f/A_f$ then the normalized cross-sectional surface PSD can be defined as;

$$\hat{s}_f(r, \vec{x}) = \frac{1}{S_f} \frac{dS_f}{d \log r}(\log r, \vec{x}) = \frac{1}{s_f A_f} \frac{dS_f}{d \log r}(\log r, \vec{x}),$$

so that the average extinction efficiency is given by

$$\langle Q_{\text{ext}} \rangle = \frac{\langle C_{\text{ext}} \rangle}{s_f} = \frac{\tau_f}{s_f} \quad (\text{B2})$$

$$\begin{aligned} &= \int_{-\infty}^{\infty} Q_{\text{ext}}(m, r, \lambda) \hat{s}_f(\log r, \vec{x}) d \log \rho \\ &\cong \int_{-\infty}^{\infty} Q_{\text{ext}}(\rho) \hat{s}_f(\log r, \vec{x}) d \log \rho \end{aligned} \quad (\text{B3})$$

where we have, for simplicity, dropped the arguments of $\langle C_{\text{ext}} \rangle$.

[45] The variable ρ is Van de Hulst's phase shift parameter = $\xi r = \frac{2\pi r}{\lambda} \times 2|m - 1|$.

[46] The three dimensional functionality of $Q_{\text{ext}}(m, r, \lambda)$ being approximated by a function of a single argument (ρ) is a manifestation of the anomalous diffraction approximation [van de Hulst, 1957].

[47] If the variation of the cross-sectional surface PSD can approximately be described by a bulk abundance and/or a log-translation increase (i.e. if it is a LTPSD as defined in Appendix A above), then;

$$\begin{aligned} \langle Q_{\text{ext}} \rangle &\cong \int_{-\infty}^{\infty} Q_{\text{ext}}(\rho) \hat{s}_f(\log r - \log r^*) d \log \rho \\ &\cong \int_{-\infty}^{\infty} Q_{\text{ext}}(\rho) \hat{s}_f\left(\log \frac{\rho}{\xi} - \log \frac{\rho^*}{\xi}\right) d \log \rho \\ &\cong \int_{-\infty}^{\infty} Q_{\text{ext}}(\rho) \hat{s}_f(\log \rho - \log \rho^*) d \log \rho \end{aligned} \quad (\text{B3a})$$

$$\cong f(\rho^*) \quad (\text{B3b})$$

where r^* is some reference radius fixed to the PSD (see the discussion in Appendix A above). This final relationship simply states that $\langle Q_{\text{ext}} \rangle$ is approximately a monotonic function of $\rho^* = \xi r^*$. We chose r^* to be the effective radius ($r_{\text{eff},f}$) parameter of Hansen and Travis [1974].

[48] To summarize, we have (in direct analogy to the anomalous diffraction approximation for mono-dispersive

aerosols) succeeded in transforming equation (B1) from a 3 dimensional function to an approximate uni-dimensional function in the specific case where the particle size distribution is an LTPSD. The multi-argument dependency has been effectively bundled into a "bulk" van de Hulst phase shift parameter given by;

$$\rho_{\text{eff},f} = \xi r^* = \frac{2\pi r_{\text{eff},f}}{\lambda} \times 2|m - 1|$$

B2. Relationships Between Spectral Derivatives and Mechanical Derivatives

[49] The claim that $\langle Q_{\text{ext}} \rangle = \tau_f/S_f \cong f(\rho_{\text{eff},f})$ for a PSD which is approximately log-translatable leads to simple expressions for the fine-mode Angstrom exponent α_f and the spectral derivative of the fine mode Angstrom exponent α'_f . The former parameter is defined as the spectral derivative in the presence of a given size distribution; if the optics of a fine mode size distribution are largely described in terms of $\rho_{\text{eff},f}$ then one can write;

$$\begin{aligned} \alpha_f &= - \left(\frac{\partial \log \langle C_{\text{ext}} \rangle}{\partial \log \lambda} \right)_{r_{\text{eff},f},m} = - \left(\frac{\partial \log \langle Q_{\text{ext}} \rangle}{\partial \log \lambda} \right)_{r_{\text{eff},f},m} \\ &= - \left(\frac{\partial \log s_f}{\partial \log \lambda} \right)_{r_{\text{eff},f},m} = - \left(\frac{\partial \log (\tau_f/S_f)}{\partial \log \lambda} \right)_{r_{\text{eff},f},m} \end{aligned} \quad (\text{B4})$$

A standard application of the chain rule then yields;

$$\begin{aligned} \alpha_f &= - \frac{d \log (\tau_f/S_f)}{d \log \rho_{\text{eff},f}} \left(\frac{\partial \log \rho_{\text{eff},f}}{\partial \log \lambda} \right)_{r_{\text{eff},f},m} = - \frac{d \log (\tau_f/S_f)}{d \log \rho_{\text{eff},f}} (-1) \\ &= \frac{d \log (\tau_f/S_f)}{d \log \rho_{\text{eff},f}} \end{aligned} \quad (\text{B5})$$

where it becomes clear that if $\tau_f/S_f \cong f(\rho_{\text{eff},f})$ then α_f is also a function of $\rho_{\text{eff},f}$. The expressions above are independent of the base of the logarithm. The spectral derivative of α_f is written;

$$\alpha'_f = \left(\frac{\partial \alpha_f}{\partial \ln \lambda} \right)_{r_{\text{eff},f},m} = \frac{d \alpha_f}{d \ln \rho_{\text{eff},f}} \left(\frac{\partial \ln \rho_{\text{eff},f}}{\partial \ln \lambda} \right)_{r_{\text{eff},f},m} = - \frac{d \alpha_f}{d \ln \rho_{\text{eff},f}} \quad (\text{B6})$$

[50] These fundamental expressions lead to some useful corollaries. From equation (B1), the fine mode optical depth increase for a given wavelength can be written;

$$d \log \tau_f = d \log \langle C_{\text{ext}} \rangle + d \log A_f$$

From equation (B2) we have

$$\begin{aligned} &= d \log \langle Q_{\text{ext}} \rangle + d \log s_f + d \log A_f \\ &= \left(\frac{\partial \log \langle C_{\text{ext}} \rangle}{\partial \log \rho_{\text{eff},f}} \right)_{\lambda} d \log \rho_{\text{eff},f} + \left(\frac{d \log s_f}{d \log r_{\text{eff},f}} + \gamma \right) d \log r_{\text{eff},f} \\ &= \alpha_f d \log \rho_{\text{eff},f} + (2 + \gamma) d \log r_{\text{eff},f} \\ &\approx (\alpha_f + 2 + \gamma) d \log r_{\text{eff},f}, \text{ or hence;} \end{aligned}$$

$$\frac{d \log \tau_f}{d \log r_{\text{eff},f}} \approx \alpha_f + 2 + \gamma \quad (\text{B7})$$

where s_f is simply proportional to $r_{\text{eff},f}^2$ for a LTPSD (see Appendix A above) and where the second last step is the result of assuming that $|m - 1|$ is largely uncorrelated with $r_{\text{eff},f}$. γ is the relative rate of increase of abundance with respect to $r_{\text{eff},f}$, viz;

$$\gamma = \frac{d \log A_f}{d \log r_{\text{eff},f}}$$

The analogous expression for the surface cross section is

$$\gamma_s = \frac{d \log S_f}{d \log r_{\text{eff},f}} = \frac{d \log s_f}{d \log r_{\text{eff},f}} + \frac{d \log A_f}{d \log r_{\text{eff},f}} = 2 + \gamma$$

It is important to keep in mind that the transformation $dy = dy/dx dx$ implies that y is a differentiable function of x over the range of aerosol particle variation chosen to evaluate the derivative. This is a condition that becomes progressively less probable as one includes a greater variety of aerosol particle events.

[51] Finally we note that if $|m - 1|$ is actually correlated to some degree with $r_{\text{eff},f}$ then equation (A7) becomes

$$\frac{d \log \tau_f}{d \log r_{\text{eff},f}} \approx \alpha_f \left(1 + \frac{d \log |m - 1|}{d \log r_{\text{eff},f}} \right) + 2 + \gamma \quad (\text{B8})$$

Notation

AOD	aerosol optical depth (τ_a).
A_f	fine mode abundance (number of particles in an atmospheric column per unit area with units of μm^{-2}).
C_{ext}	average extinction cross section of a single aerosol particle (typical units of cm^2 or μm^2).
α_f	instantaneous slope of $-\ln \tau_f$ vs $\ln \lambda$
α	instantaneous slope of $-\ln \tau_a$ vs $\ln \lambda$
α'_f	instantaneous slope of α_f vs $\ln \lambda$
α'	instantaneous slope of α vs $\ln \lambda$
λ	wavelength [nm].
log, ln	\log_{10} and natural log.
LTPSD	log-translatable PSD (Appendix A).
m	complex refractive index.
ω_o	single scattering albedo.
σ	geometric standard deviation of a lognormal frequency distribution. If $\text{stdev}(\log x)$ represents the standard deviation of a distribution of parameter x on a log scale, then $\sigma = 10^{\text{stdev}(\log x)}$. Note that $\sigma = \exp(\sigma_g)$ of Hansen and Travis [1974].
σ_A	geometric standard deviation of an abundance distribution $dA/d\ln r$.
σ_S	geometric standard deviation of a (cross sectional) distribution $dS/d\ln r$.
σ_V	geometric standard deviation of a volume distribution $dV/d\ln r$.
PSD	particle size distribution.
Q_{ext}	average extinction efficiency = C_{ext}/s .
R^2	square of the correlation coefficient for a linear regression.
r_3	average radius of a size distribution; v , the average particle volume = $4/3\pi r_3^3$.

r_{eff}	optically effective radius of a size distribution in μm ($= r_g \exp(2.5 \ln^2 \sigma)$) for a log-normal size distribution, <i>ibid</i>).
$r_{\text{eff},f}$	optically effective radius of the fine mode.
$r_{\text{eff},f,2}$	$r_{\text{eff},f,2}$ is the effective radius of the larger fine-mode component for a bi-modal fine-mode size distribution
$\rho_{\text{eff},f}$	effective phase shift parameter of the fine mode. $\rho_{\text{eff},f,2}$ is the analogue of $r_{\text{eff},f,2}$.
r_A	geometric mean of an abundance distribution $dA/d\ln r$.
r_S	geometric mean of a (cross sectional) distribution $dS/d\ln r$.
r_V	geometric mean of a volume distribution $dV/d\ln r$.
r_g	geometric radius of a log-normal particle size size distribution in μm (<i>ibid</i>)
S_f	fine mode cross sectional surface PSD (cross sectional area of all particles in an atmospheric column per unit area). Unitless [$\mu\text{m}^2 \cdot \mu\text{m}^{-2}$].
s_f	average cross sectional area per particle for the fine mode PSD ($s_f = S_f/A_f$).
t	trajectory time [days].
τ_f	fine mode optical depth.
τ_a	total aerosol optical depth (AOD).

[52] Note that all optical quantities are referenced to 500 nm wavelength unless otherwise indicated. Parameters are unitless unless otherwise indicated.

[53] **Acknowledgments.** The authors would like to thank the National Aeronautics and Space Administration (NASA), the National Sciences and Engineering Research Council of Canada (NSERC) and the Canadian Foundation for Climate and Atmospheric Sciences (CFCAS) for their financial support. The lead author is especially indebted to Brent Holben at GSFC/NASA as well as Bob Curran at GEST/UMBC (Goddard Earth Sciences and Technology Center at the University of Maryland at Baltimore County) for providing a senior visiting research position. Valuable in-kind support was obtained from the Meteorological Services of Canada (MSC) and the AERONET project. The contributions of Jim Freemantle, the AEROCAN coordinator and Egbert technical manager, Ilya Slutsker and David Gilles of the AERONET group and Alain Royer the co-PI of the AEROCAN network are gratefully acknowledged. Acknowledgments are also due to the PIs at the different AERONET sites employed in this study; Glen Lesins at Halifax, NS, Jay Herman, Maria Tzortziou, and Gordon Labow at SERC (Smithsonian Environmental Research Center) in Edgewater, MD, and Brent Holben the PI at CCNY (City College of New York) NY, COVE (CERES Ocean Validation Experiment) near Virginia Beach, VA, Howland, ME, MDSC (Maryland Science Center), Wallops Island VA, Norfolk, VA, and GSFC, MD. Finally, we would like to gratefully acknowledge the constructive criticisms of one reviewer concerning the importance of NO_2 absorption to the derived optical statistics.

References

- Colarco, P. R., M. R. Schoeberl, B. G. Doddridge, L. T. Marufu, O. Torres, and E. J. Welton (2004), Transport of smoke from Canadian forest fires to the surface near Washington, D. C.: Injection height, entrainment, and optical properties, *J. Geophys. Res.*, *109*, D06203, doi:10.1029/2003JD004248.
- Draxler, R. R., and G. D. Rolph (2003), HYSPLIT (HYbrid Single-Particle Lagrangian Integrated Trajectory) Model access via NOAA ARL READY Website, Air Resour. Lab., Natl. Oceanic and Atmos. Admin., Silver Spring, Md. (Available at <http://www.arl.noaa.gov/ready/hysplit4.html>)
- Dubovik, O., and M. D. King (2000), A flexible inversion algorithm for retrieval of aerosol optical properties from Sun and sky radiance measurements, *J. Geophys. Res.*, *105*, 20,673–20,696.
- Dubovik, O., A. Smirnov, B. N. Holben, M. D. King, Y. J. Kaufman, T. F. Eck, and I. Slutsker (2000), Accuracy assessments of aerosol optical properties retrieved from AERONET sun and sky-radiance measurements, *J. Geophys. Res.*, *105*, 9791–9806.
- Eck, T. F., B. N. Holben, J. S. Reid, O. Dubovik, A. Smirnov, N. T. O'Neill, I. Slutsker, and S. Kinne (1999), The wavelength dependence of the

- optical depth of biomass burning, urban, and desert dust aerosols, *J. Geophys. Res.*, *104*, 31,333–31,350.
- Eck, T. F., B. N. Holben, D. E. Ward, O. Dubovik, J. S. Reid, A. Smirnov, M. M. Mukelabai, N. C. Hsu, N. T. O'Neill, and I. Slutsker (2001), Characterization of the optical properties of biomass burning aerosols in Zambia during the 1997 ZIBBEE field campaign, *J. Geophys. Res.*, *106*(D4), 3425–3448.
- Hansen, J. E., and L. D. Travis (1974), Light scattering in planetary atmospheres, *Space Sci. Rev.*, *16*, 527–610.
- Holben, B. N., A. Setzer, T. F. Eck, A. Pereira, and I. Slutsker (1996), Effect of dry-season biomass burning on Amazon basin aerosol concentrations and optical properties, 1992–1994, *J. Geophys. Res.*, *101*(D14), 19,465–19,481.
- Martin, R. V., D. J. Jacob, K. Chance, T. P. Kurosu, P. I. Palmer, and M. J. Evans (2003), Global inventory of nitrogen oxide emissions constrained by space-based observations of NO₂ columns, *J. Geophys. Res.*, *108*(D17), 4537, doi:10.1029/2003JD003453.
- O'Neill, N. T., T. F. Eck, B. N. Holben, A. Smirnov, A. Royer, and Z. Li (2002), Optical properties of boreal forest fire smoke derived from sunphotometry, *J. Geophys. Res.*, *107*(D11), 4125, doi:10.1029/2001JD000877.
- O'Neill, N., T. F. Eck, A. Smirnov, B. N. Holben, and S. Thulasiraman (2003), Spectral discrimination of coarse and fine mode optical depth, *J. Geophys. Res.*, *108*(D17), 4559, doi:10.1029/2002JD002975.
- Reid, J. S., P. V. Hobbs, R. J. Ferek, D. R. Blake, J. V. Martrins, M. R. Dunlap, and C. Liou (1998), Physical, chemical, and optical properties of regional hazes dominated by smoke in Brazil, *J. Geophys. Res.*, *103*, 32,059–32,080.
- Reid, J. S., T. F. Eck, S. A. Christopher, P. V. Hobbs, and B. N. Holben (1999), Use of the Ångström exponent to estimate the variability of optical and physical properties of aging smoke particles in Brazil, *J. Geophys. Res.*, *104*, 27,473–27,489.
- Reid, J. S., E. M. Prins, D. L. Westphal, C. C. Schmidt, K. A. Richardson, S. A. Christopher, T. F. Eck, E. A. Reid, C. A. Curtis, and J. P. Hoffman (2004), Real-time monitoring of South American smoke particle emissions and transport using a coupled remote sensing/box-model approach, *Geophys. Res. Lett.*, *31*, L06107, doi:10.1029/2003GL018845.
- Remer, L. A., Y. J. Kaufman, B. N. Holben, A. M. Thompson, and D. McNamara (1998), Biomass burning aerosol size distribution and modeled optical properties, *J. Geophys. Res.*, *103*(D4), 31,879–31,891.
- Shaw, G. E. (1976), Nitrogen dioxide - optical absorption in the visible, *J. Geophys. Res.*, *81*, 5791–5792.
- Smirnov, A., B. N. Holben, T. F. Eck, O. Dubovik, and I. Slutsker (2000), Cloud screening and quality control algorithms for the AERONET database, *Remote Sens. Environ.*, *73*, 337–349.
- Taubman, B. F., L. T. Marufu, B. L. Vant-Hull, C. A. Piety, B. G. Doddridge, R. R. Dickerson, and Z. Li (2004), Smoke over haze: Aircraft observations of chemical and optical properties and the effects on heating rates and stability, *J. Geophys. Res.*, *109*, D02206, doi:10.1029/2003JD003898.
- Thomas, W., E. Hegels, S. Slijkhuis, R. Spurr, and K. Chance (1998), Detection of biomass burning combustion products in Southeast Asia from backscatter data taken by the GOME spectrometer, *Geophys. Res. Lett.*, *25*, 1317–1320.
- van de Hulst, H. C. (1957), *Light Scattering by Small Particles*, 470 pp., John Wiley, Hoboken, N. J.
- Welton, E. J., J. R. Campbell, J. D. Spinhirne, and V. S. Scott (2001), Global monitoring of clouds and aerosols using a network of micro-pulse lidar systems, in *Lidar Remote Sensing for Industry and Environmental Monitoring*, edited by U. N. Singh, T. Itabe, and N. Sugimoto, *Proc. SPIE*, *4133*, 151.

T. F. Eck, NASA Goddard Space Flight Center, Greenbelt, MD 20771, USA.

N. T. O'Neill and S. Thulasiraman, CARTEL, Université de Sherbrooke, Sherbrooke, Québec, Canada J1K 2R1. (norm.oneill@usherbrooke.ca)

J. S. Reid, Naval Research Laboratory, Monterey, CA 93943-5502, USA.

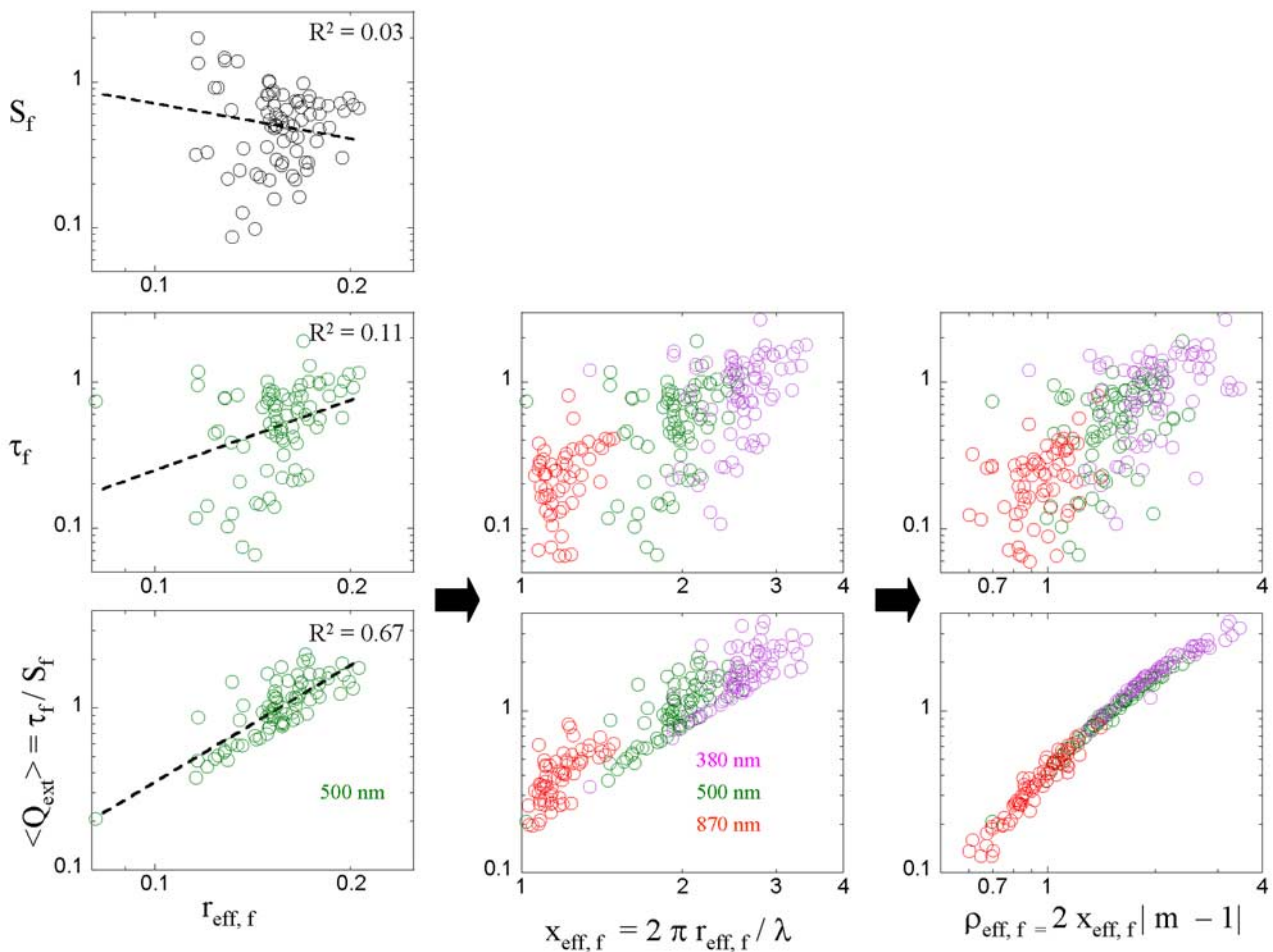


Figure 2a. Demonstration of the approach to a nearly monotonic dependence of $\langle Q_{\text{ext}} \rangle = \tau_f/S_f$ on $\rho_{\text{eff},f}$ for a representative data set (extracted from or computed from AERONET inversion data from Norfolk, VA, during July of 2002). The first column of graphs (vs $r_{\text{eff},f}$) are restricted to computations at 500 nm while the 2nd and 3rd column of graphs (vs $x_{\text{eff},f}$ and $\rho_{\text{eff},f}$ respectively) are plotted for 380, 500 and 870 nm.

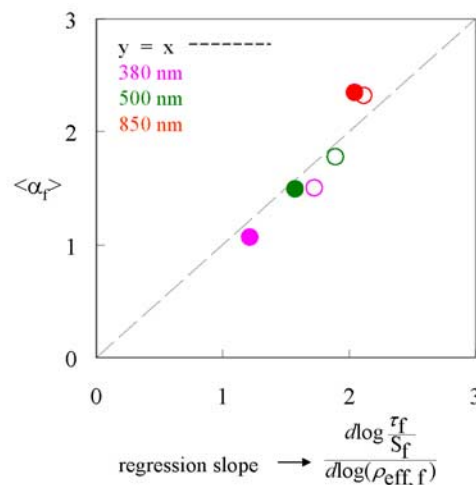


Figure 2b. Average value of α_f (extracted by fitting a second order polynomial to the AERONET inversion value of τ_f) as a function of α_f extracted from the regression slope of the τ_f/S_f versus $\rho_{\text{eff},f}$ points in Figure 2a. The two points per wavelength result from dividing the AOD data into regimes of $r_{\text{eff},f} < 0.159$ (open circular symbols) and $r_{\text{eff},f} > 0.159 \mu\text{m}$ (solid circular symbols). The cutoff of $0.159 \mu\text{m}$ represents the average value of $r_{\text{eff},f}$ for the ensemble of Norfolk, July 2002 data.

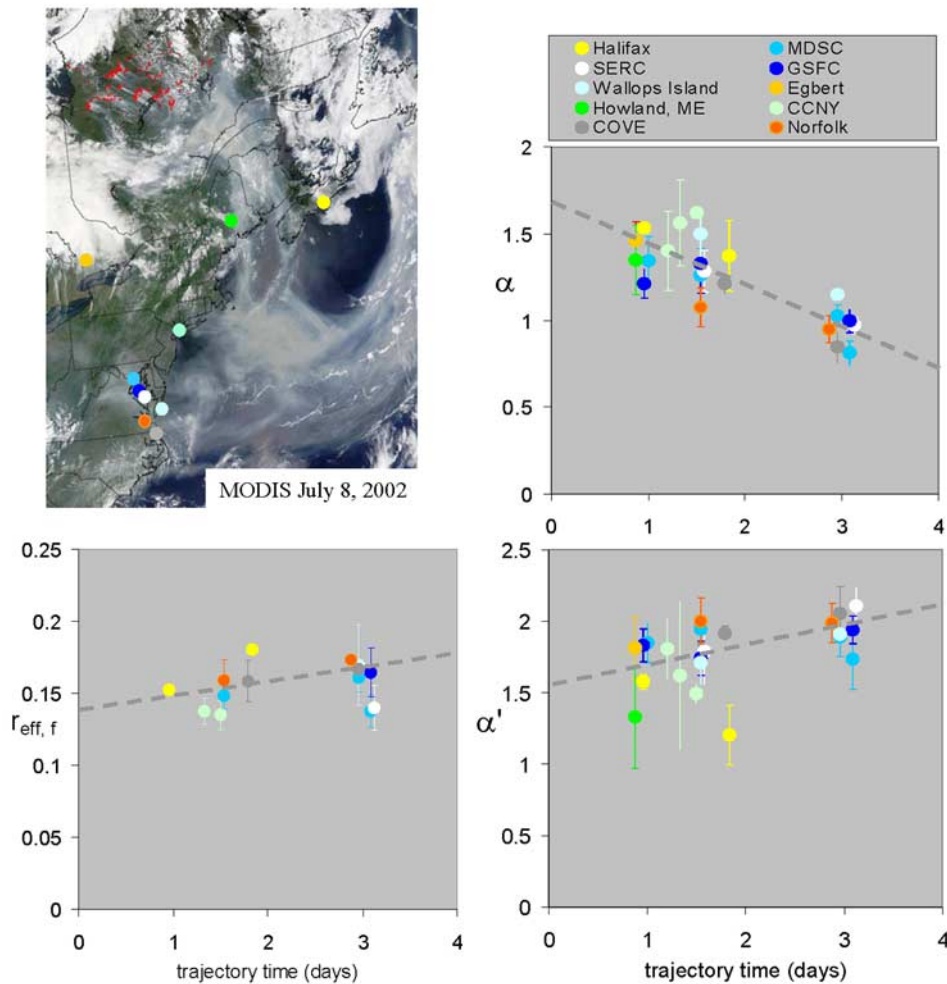


Figure 4. Sample MODIS image along with graphs of α , α' and $r_{\text{eff},f}$ as a function of trajectory time (t) for all sunphotometer sites where data were acquired during the Québec smoke event (see Table 1 for site data). α and α' were computed at the reference wavelength of 500 nm. The red markings on the MODIS image show fire source locations. The grey dashed lines represent overall regression lines. Each point and its error bar is an average and standard deviation of all sunphotometry data acquired for ± 6 hours on either side of the nominal trajectory arrival time. The $r_{\text{eff},f}$ versus t graph has fewer points than the α versus t and the α' versus t graphs because not all extinction measurement time windows encompassed an inversion time. In addition each point of the $r_{\text{eff},f}$ versus t graph represents fewer measurements since inversions were relatively rare (see Table 2).

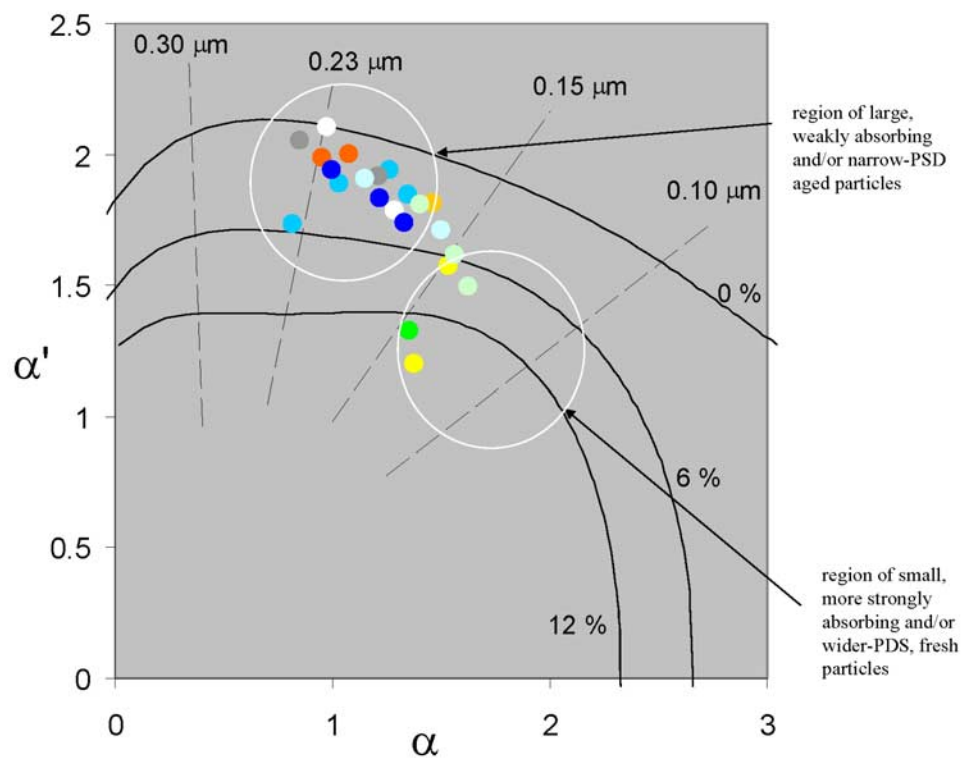


Figure 5. α' vs α for the Québec smoke event (same station colors and symbols as for Figure 4). Superimposed on the data are the simulated Mie curves defined in the caption of Figure 1.

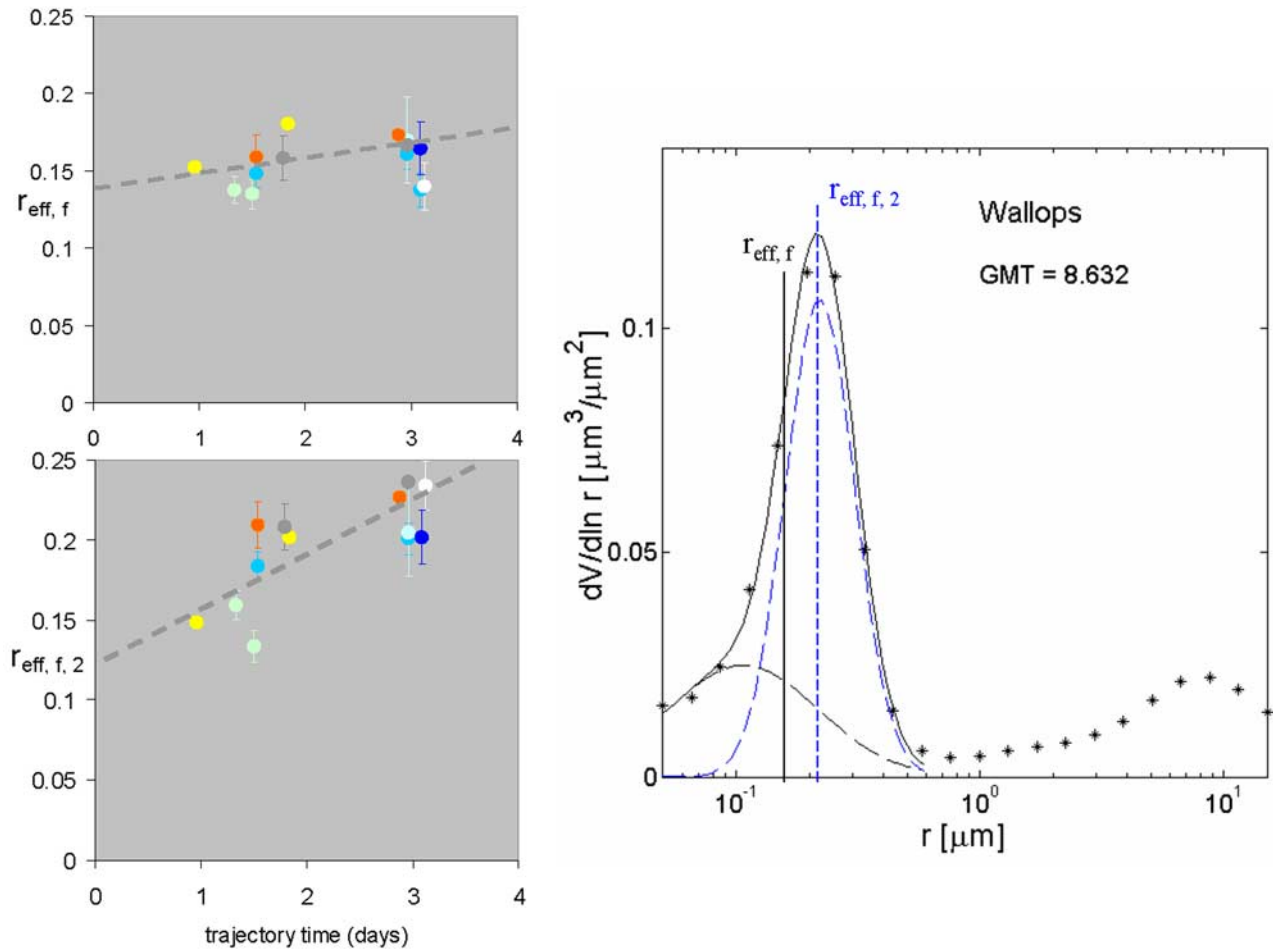


Figure 6a. Variation of $r_{\text{eff},f,2}$ (the effective radius of the larger-radius mode of the fine mode PSD) as a function of trajectory time, alongside the original variation of $r_{\text{eff},f}$ from Figure 4. The rightmost graph is an illustration of the biomodal fitting procedure which was applied to the AERONET inversion PSDs to yield $r_{\text{eff},f,2}$. In this latter figure the asterisks represent the data while the dashed curves represent the bi-modal components of the total fitted (solid line) curve.

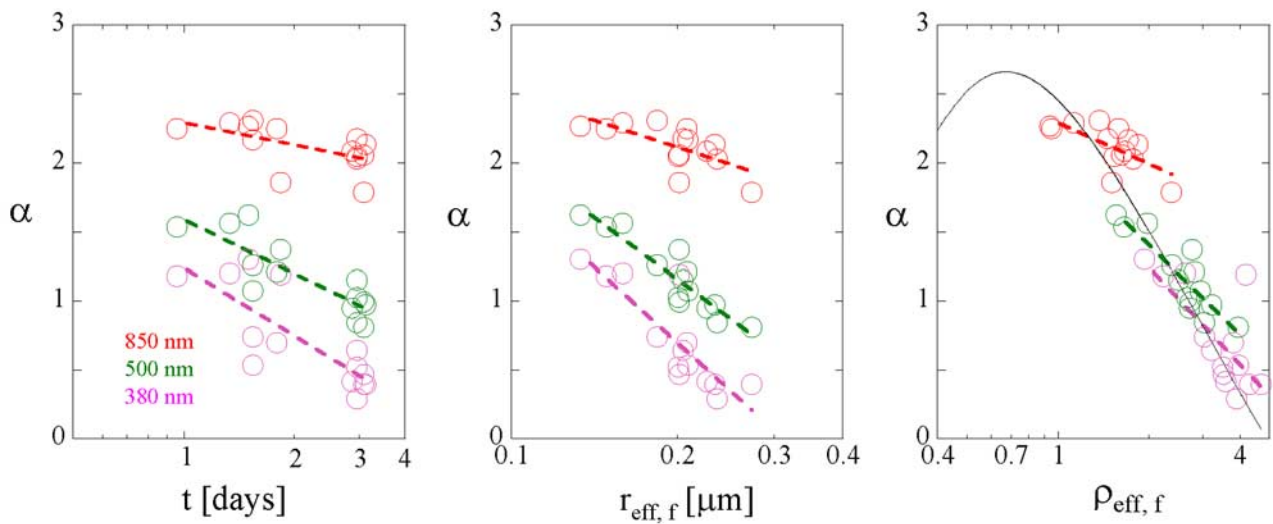


Figure 7. α vs trajectory time (t), $r_{\text{eff},f,2}$ and $\rho_{\text{eff},f,2}$ for the Québec smoke event data. The points are the result of the 6 hour averages which encompass the inversion times of the $r_{\text{eff},f}$ versus t graph of Figure 4 (the 500 nm points are a subset of the set of points seen on the α versus t graphs of Figure 4).